

# Probing the Inner Circumgalactic Medium and Quasar Illumination around the Reddest ‘Extremely Red Quasar’ (ERQ)

Marie Wingyee Lau,<sup>1\*</sup> Fred Hamann,<sup>1</sup> Jarred Gillette,<sup>1</sup> Serena Perrotta,<sup>2</sup> David S. N. Rupke,<sup>3</sup> Dominika Wylezalek<sup>4</sup> and Nadia L. Zakamska<sup>5,6</sup>

<sup>1</sup>*Department of Physics & Astronomy, University of California, Riverside, CA 92521, USA*

<sup>2</sup>*Center for Astrophysics and Space Sciences, University of California, San Diego, CA 92093, USA*

<sup>3</sup>*Department of Physics, Rhodes College, Memphis, TN 38112, USA*

<sup>4</sup>*Astronomical Calculation Institute, University of Heidelberg, D-69120 Heidelberg, Germany*

<sup>5</sup>*Department of Physics & Astronomy, Johns Hopkins University, Baltimore, MD 21218, USA*

<sup>6</sup>*Institute for Advanced Study, Princeton, NJ 08540, USA*

Accepted XXX. Received YYY; in original form ZZZ

## ABSTRACT

Dusty quasars might be in a young stage of galaxy evolution with prominent quasar feedback. A recently discovered population of luminous, extremely red quasars at  $z \sim 2\text{--}4$  has extreme spectral properties related to exceptionally powerful quasar-driven outflows. We present Keck/KCWI observations of the reddest known ERQ, at  $z = 2.3184$ , with extremely fast [O III]  $\lambda 5007$  outflow at  $\sim 6000 \text{ km s}^{-1}$ . The Ly $\alpha$  halo spans  $\sim 100 \text{ kpc}$ . The halo is kinematically quiet, with velocity dispersion  $\sim 300 \text{ km s}^{-1}$  and no broadening above the dark matter circular velocity down to the spatial resolution  $\sim 6 \text{ kpc}$  from the quasar. We detect spatially-resolved He II  $\lambda 1640$  and C IV  $\lambda 1549$  emissions with kinematics similar to the Ly $\alpha$  halo and a narrow component in the [O III]  $\lambda 5007$ . Quasar reddening acts as a coronagraph allowing views of the innermost halo. A narrow Ly $\alpha$  spike in the quasar spectrum is inner halo emission, confirming the broad C IV  $\lambda 1549$  in the unresolved quasar is blueshifted by  $2240 \text{ km s}^{-1}$  relative to the halo frame. We propose the inner halo is dominated by moderate-speed outflow driven in the past and the outer halo dominated by inflow. The high central concentration of the halo and the symmetric morphology of the inner region are consistent with the ERQ being in earlier evolutionary stage than blue quasars. The He II  $\lambda 1640$ /Ly $\alpha$  ratio of the inner halo and the asymmetry level of the overall halo are dissimilar to Type II quasars, suggesting unique physical conditions for this ERQ that are beyond orientation differences from other quasar populations. We find no evidence of mechanical quasar feedback in the Ly $\alpha$ -emitting halo.

**Key words:** quasars: emission lines – quasars: individual: SDSS J000610.67+121501.2 – galaxies: intergalactic medium – galaxies: haloes – galaxies: evolution – galaxies: high-redshift

## 1 INTRODUCTION

Quasars are phenomena of rapid accretion onto supermassive black holes in the centres of massive galaxies, that can regulate the evolution of their host galaxies via feedback processes. Popular models of galaxy evolution predict that supermassive black holes initially grow in obscurity, deep inside dusty galactic starbursts, until they are massive enough to power quasars (Sanders et al. 1988; Hopkins et al. 2008). Outflows from the quasars then drive major blowouts of gas and dust, which quench star formation and reveal visibly luminous quasars in the galactic nuclei (Hopkins & Elvis 2010; Liu et al. 2013). At high redshifts, gaseous infalls from the intergalactic medium, e.g. cold-mode accretion, may be the dominant mechanism for feeding the build-up of galaxy masses, triggering starbursts, and fueling quasar activities (Kereš et al. 2009; Dekel et al. 2009; Fumagalli et al. 2014). It is likely that infall and outflow occur together

whenever high-redshift galaxy assembly via cold-mode accretion is accompanied by major starburst and quasar activity (Costa et al. 2014; Nelson et al. 2015; Suresh et al. 2019).

Dust obscured, reddened quasars provide important tests of quasar/galaxy evolution models, because they are expected to be young objects, appearing during the brief blowout, transition phase between the initial dusty starbursts and later normal blue quasars. Dusty quasars are prime candidates for searching for signs of early stages of evolution. Such signs may include higher supermassive black hole accretion rates relative to Eddington, more common or more powerful outflows and feedback driven by the quasars, and/or more active inflows from the intergalactic medium. Various dusty quasar populations have been selected using a range of colour and brightness criteria, in e.g. Canalizo & Stockton (2001), Urrutia et al. (2008), Glikman et al. (2022), Assef et al. (2015), and Banerji et al. (2015). All of these populations appear to require more extreme, powerful physical properties beyond what could be attributed to orientation effects in the unified model for active galactic nuclei (An-

\* E-mail: wingyeel@ucr.edu (MWL)

tonucci 1993; Netzer 2015). Dusty quasars are unique laboratories to study quasar/galaxy evolution also by the virtue of being the dominant population of the first quasars. It is predicted that >50 per cent of quasars at the epoch of reionization have most of their UV radiation obscured by dust (Di Mascia et al. 2021; Ni et al. 2022). Because cosmological dimming has a steep dependence on redshift and the first quasars are rare, dusty quasars at the highest redshifts are still missing in current systematic searches (Connor et al. 2019; Vito et al. 2019).

Hamann et al. (2017) followed up the initial work of Ross et al. (2015) and refined the discovery of a population of ‘extremely red quasars’ (ERQs). ERQs are selected from sources in the twelfth data release of the Baryon Oscillation Spectroscopic Survey (BOSS, Pâris et al. 2017) in the Sloan Digital Sky Survey-III (SDSS, Eisenstein et al. 2011) matched to sources in the ALLWISE data release (Cutri et al. 2013) of the Wide-field Infrared Survey Explorer (WISE, Wright et al. 2010). More than 300 sources are selected, based on extremely red colour from the rest-frame UV to mid-IR of  $i - W3 > 4.6$  AB mag. ERQs are at cosmic noon redshifts  $z \sim 2-4$ , and have high bolometric luminosities  $L_{\text{bol}} \gtrsim 10^{47} \text{ erg s}^{-1}$ .

The BOSS rest-frame UV spectra reveal that ERQs have exotic spectral properties unlike any other known quasar populations. They have a high incidence of blueshifted broad absorption lines and large emission-line blueshifts. They have a high incidence of unusually strong broad emission lines with C IV  $\lambda 1549$  rest equivalent width often exceeding  $100 \text{ \AA}$ , and the broad emission lines tend to have peculiar profiles that are wingless with high kurtosis (Monadi & Bird 2022). They have a high incidence of unusual broad emission line flux ratios such as high N V  $\lambda 1240$ /C IV  $\lambda 1549$  and high N V  $\lambda 1240$ /H I Ly $\alpha$ . These features emphasize small-scale outflow phenomena controlled by accretion physics, on scales of tens of pc (Zhang et al. 2017; Alexandroff et al. 2018). Rest-frame optical spectra in Zakamska et al. (2016) and Perrotta et al. (2019) reveal that ERQs have the broadest and most blueshifted [O III]  $\lambda 5007$  emission lines ever reported, reaching  $>6000 \text{ km s}^{-1}$  and are strongly correlated with the red colours. The [O III] lines are significant because they trace gas on galactic scales, being low-density forbidden transitions (Hamann et al. 2011). These [O III]-emitting outflows carry enough kinetic energy to drive important feedback in the host galaxies. The extreme [O III]  $\lambda 5007$  and broad emission line properties in ERQs appear to require more extreme physical properties than other quasars that are beyond orientation differences.

Hamann et al. (2017) also note that narrow Ly $\alpha$  emission ‘spikes’ are often seen in the BOSS spectra. The origin of these unusual spikes are speculated to be gas on larger scales than the broad-line region. Their high incidence in ERQ spectra is possibly caused by extinction of the direct central quasar light. The spikes are then important redshift indicators, especially in ERQs where broad emission line blueshifts appear common and estimates of the systemic redshifts from the broad lines are unreliable.

The known prodigious outflows support the hypothesis that ERQs are candidate young quasars, tied to an early, powerful stage of quasar-galaxy evolution, as have been inferred for the hot dust-obscured galaxies (hot DOGs, Noboriguchi et al. 2019; Finnerty et al. 2020). Observations of ERQ host galaxies and their extended environments are needed to test this hypothesis. The host galaxies of ERQs are explored in Zakamska et al. (2019) using direct *Hubble Space Telescope* images with a goal of identifying signs of early stages of evolution. Somewhat surprisingly, they found no evidence of enhanced major merger activities relative to luminosity- and redshift-matched blue quasars. However, disturbances in the host galaxies may be hidden by the inherent difficulty in subtracting the quasar point-spread function

in two-dimensional images especially at high redshifts. Vayner et al. (2021) used adaptive optics-assisted integral field spectroscopy to confirm that the [OIII]-emitting outflows happen on  $\sim 1 \text{ kpc}$  scales and carry enough momenta to clear the nuclear regions of their host galaxies. To explore whether the ERQ-driven outflows have detectable impact on the larger, circumgalactic scales, one may employ wide-field integral field spectrographs, such as the Keck Cosmic Web Imager (KCWI, Morrissey et al. 2018) on the Keck II telescope. The circumgalactic medium is loosely defined as the gaseous halo extending out to  $\sim 300 \text{ kpc}$  from the central galaxy (Lau et al. 2016; Tumlinson et al. 2017). It is the site of interplay between outflows from and accretion onto the galaxy it surrounds, and has significant impact on the evolution of the galaxy.

Massive gas reservoirs around high-redshift quasars have been detected via fluorescent Ly $\alpha$  emission. Around mostly radio-quiet, luminous blue quasars, emission-line regions of linear extents  $\sim 100 \text{ kpc}$  are frequently detected around statistical samples of them, using wide-field integral field spectrographs on 8m class telescopes (Borisova et al. 2016; Arrigoni Battaia et al. 2019; Cai et al. 2019). They are often interpreted as tracing filamentary, inflowing gas of cold-mode accretion. For radio-quiet obscured quasars, extended line emissions have been detected around sources selected using various methods, using mixed observing techniques on telescopes of various apertures to various exposure depths. (Bridge et al. 2013; Prescott et al. 2015a,b; Cai et al. 2017; den Brok et al. 2020; Herenz et al. 2020; O’Sullivan et al. 2020; Li et al. 2022; Sanderson et al. 2021). ERQs selected from the BOSS quasar catalogue are a well-defined and uniform sample. They are thus ideal targets to advance Ly $\alpha$  halo studies beyond random surveys (e.g., Borisova et al. 2016; Arrigoni Battaia et al. 2019; Cai et al. 2019) or exotic single objects (e.g., Cantalupo et al. 2014; Ginolfi et al. 2018; Li et al. 2019) to tests of quasar/galaxy evolution that are both statistical and specific.

Our team is currently building a KCWI sample of ERQs. In this paper we report results on the reddest of all known ERQs, SDSS J000610.67+121501.2, hereafter J0006+1215. It has a rest-frame UV to mid-IR colour of  $i - W3 = 8.01$  AB mag, an emission redshift of  $z_{\text{em}} = 2.3184$ , and is radio quiet. The first goal relates to the circumgalactic medium and quasar illumination pattern. We will test whether the extended line emissions have unusual properties that may relate to the quasar obscuration, and/or a younger, more active, blowout phase of evolution. We will search for differences compared to the more extensively studied luminous blue quasars at similar redshifts, which are expected to be more evolved. The second goal relates to using the Ly $\alpha$  halo to estimate the systemic redshift. We will test the assertion that the Ly $\alpha$  spike in the BOSS spectrum is halo emission at the systemic redshift, that can be used to study the apparently very large blueshifts of the broad emission lines.

This paper is organized as follows. Section 2 describes the selection of J0006+1215, its observation, data reduction, and post-processing. Section 3 describes the spectral properties of the J0006+1215 quasar, extraction of the extended line emissions, and analysis results of size, morphology, surface brightness, and kinematics of the extended emissions. Section 4 discusses the implications for quasar feedback, circumgalactic medium, and quasar studies. Section 5 concludes the paper. Throughout this paper we adopt a  $\Lambda$  cold dark matter cosmology with  $H_0 = 69.6 \text{ km s}^{-1} \text{ Mpc}^{-1}$ ,  $\Omega_{\text{M}} = 0.286$ , and  $\Omega_{\Lambda} = 0.714$ , as adopted by the online cosmology calculator developed by Wright (2006) at the time of this writing. We use photometric magnitudes in the AB system. We report vacuum wavelengths in the heliocentric frame. When referring to broad, blended doublet emission of C IV, we use the notation C IV  $\lambda 1549$ , and when referring to narrow, resolved doublet emission of C IV, we use the notation C IV  $\lambda\lambda 1548, 1550$ .

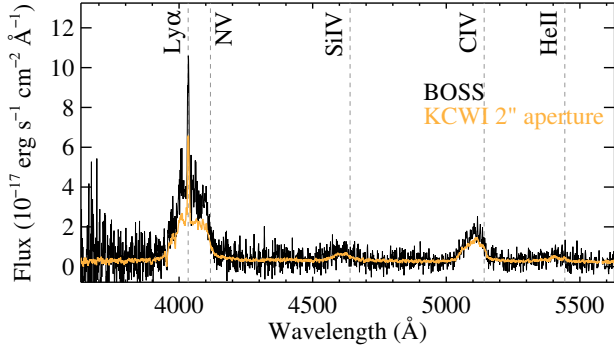


**Figure 1.** The BOSS spectrum of the quasar taken in 2011, compared to the KCWI spectrum of the quasar taken in 2019 and extracted with a matching aperture.

## 2 TARGET SELECTION, OBSERVATION, AND DATA REDUCTION

We provide details on the selection of J0006+1215, its KCWI observation, data reduction, and post-processing including modelling the quasar point-spread function.

### 2.1 J0006+1215 Selection and Basic Properties

For this first wide-field integral-field study of an ERQ, we choose the reddest among all known ERQs, with  $i - W3 = 8.01$ , which also has among the most blueshifted and broadest [O III] lines among ERQs. As measured by Perrotta et al. (2019) in a one-dimensional spectrum, the velocity shift that encompasses 98 per cent of its [O III]  $\lambda 5007$  emission-line flux integrating from the red side  $v_{98, [\text{O III}]}$  =  $-6092 \text{ km s}^{-1}$ , and the velocity width encompassing 90 per cent of the [O III] line power  $w_{90, [\text{O III}]}$  =  $6206 \text{ km s}^{-1}$ . For reference, the most extreme  $v_{98, [\text{O III}]}$  and  $w_{90, [\text{O III}]}$  measured in ERQs are  $\sim 7000 \text{ km s}^{-1}$ . We note that a narrow emission component of Ly $\alpha$  is present in the BOSS spectrum, as shown in Fig. 1, and this feature is extensively compared with halo properties in later sections.

The absolute  $i$  magnitude  $K$ -corrected to  $z \sim 2$  is a commonly used measure of the rest-frame UV luminosity of quasars. We follow the formulae for  $K$ -corrections in Ross et al. (2013) and calculate that J0006+1215 has  $M_i(z = 2) = -24.16$ . Hamann et al. (2017) estimate that ERQs are typically suppressed by three magnitudes in the rest-frame UV compared to the spectral energy distributions of normal blue quasars. J0006+1215 is suppressed by about six magnitudes in the rest-frame UV, and we estimate its intrinsic bolometric luminosity from mid-IR photometry assuming a standard Type I spectral energy distribution. We apply a bolometric correction factor of 8 to the rest-frame  $5 \mu\text{m}$  luminosity extrapolated from the  $W3$  band photometry, with details in Perrotta et al. (2019). J0006+1215 has an intrinsic bolometric luminosity of  $L_{\text{bol}} = 10^{47.9} \text{ erg s}^{-1}$ , and is near the high end of the ERQ population. The radio luminosity of J0006+1215 is in the quiet regime, and is unresolved on  $\sim 10 \text{ kpc}$  scale (Hwang et al. 2018). The X-ray spectrum of J0006+1215 indicates a Compton-thin absorbing column (Goulding et al. 2018), which is discussed in Section 4.5 regarding quasar illumination.

### 2.2 Observing

We observed J0006+1215 with Keck/KCWI on 2019 October 2. The seeing was variable with full-width-at-half-maximum (FWHM) between (0.8–1.4) arcsec, which correspond to (7–12) kpc at the quasar’s redshift. The observing conditions were photometric. We configured KCWI with the BL grating and the medium slicer, which yields a field of view of  $15.7 \text{ arcsec} \times 18.9 \text{ arcsec}$ , with slices along the long direction. At the emission redshift of the quasar, this field of view corresponds to a physical area of  $131 \text{ kpc} \times 158 \text{ kpc}$ . With 24 slicers, the instrument configuration provides a spatial sampling of  $0.68 \text{ arcsec}$  across the slices and is seeing limited along the slicers. Consecutive exposures were dithered  $0.35 \text{ arcsec}$  along slices to sub-sample the long spatial dimension of the output spaxels which have sizes of  $0.68 \text{ arcsec} \times 0.29 \text{ arcsec}$ . The spectral resolution is  $R = 1800$ . The full spectral range is (3500–5625)  $\text{\AA}$ , and covers Ly $\alpha$ , C IV  $\lambda 1549$ , and He II  $\lambda 1640$  of the quasar in observer’s frame. The total exposure time was 70 min. We obtained three exposures of 20 minutes, and one exposure of 10 minutes which was read out early due to fog. We observed an unsaturated standard star GD50 at the end of the night for flux calibration.

### 2.3 Reducing the Data

We reduce the data of the individual science exposures with the standard KCWI Data Extraction and Reduction Pipeline (KDERP, <https://github.com/Keck-DataReductionPipelines/KcwiDRP>) written in the Interactive Data Language (IDL), whose final outputs are data cubes of two spatial dimensions and one spectral dimension. We then use the IDL library IFSRED (Rupke 2014) to resample and mosaic the data cubes. The output data cubes from KDERP have rectangular spaxels, and they are resampled onto a  $0.29 \text{ arcsec} \times 0.29 \text{ arcsec}$  spaxel grid. Spaxel coordinates of the centroid of the quasar is calculated for each resampled data cube. The individual data cubes are then aligned using the position of the quasar centroid and median-combined. There are no prominent skyline residuals near the lines we investigate.

We then verify the reliability of the flux calibration. The bandpass of the KCWI data approximately matches the SDSS photometric  $g$  band, hence the SDSS  $g$  magnitude of the quasar can be used as a baseline for comparison. We extract a source spectrum from a circular aperture of 3 arcsec in diameter that is centred on the quasar in the KCWI data. This aperture is two times the seeing disc FWHM and is sufficiently large to encompass most of the source emission. We then filter the KCWI source flux spectrum with the SDSS  $g$ -band response function and integrated over the entire wavelength range. The integrated flux is converted to magnitude and is found to be  $g_{\text{KCWI}} = 22.26$ , and is 8 per cent fainter compared to the magnitude reported in SDSS  $g_{\text{SDSS}} = 22.16$ . Given quasar variability, We verify the flux calibration using the standard star as well. For the standard star, the  $g$ -band flux integrated from the KCWI spectrum is merely 2 per cent smaller than the SDSS  $g$ -band flux. We hence only report uncertainties on the flux measurements as output from KDERP and assume there are no additional unaccounted systematic uncertainties in flux calibration. The final data cube results in a  $1\sigma$  surface brightness limit of  $2.2 \times 10^{-19} \text{ erg s}^{-1} \text{ cm}^{-2} \text{ arcsec}^{-2}$  in a 1-arcsec aperture in a single 1  $\text{\AA}$  channel at the Ly $\alpha$  wavelength at the quasar’s redshift. The root-mean-square of surface brightness in a 1-arcsec aperture is  $2.0 \times 10^{-19} \text{ erg s}^{-1} \text{ cm}^{-2} \text{ arcsec}^{-2}$  for a channel in rest-frame wavelengths between 1255  $\text{\AA}$  and 1275  $\text{\AA}$ , a range with no prominent emission lines from the quasar.

## 2.4 Modelling the Point Spread Function and Other Post-Processing

We further process the data cube using the Python package CWITools (O’Sullivan & Chen 2020) for subtracting instrumental scattered light and foreground sources. We mask all continuum sources and median-filter the data cube as an estimate of instrumental scattered light and subtract it. On the basis that the point-spread function does not vary strongly as a function of wavelength, as empirically verified, we fit empirical point-spread functions or Moffat functions to foreground continuum sources. We then subtract these fits to foreground sources. We then process the spectrum in each spaxel of the data cube using the IDL library IFSFIT (Rupke & To 2021). We generate a spatially-unresolved quasar spectral template of continuum plus broad emission line components that is described in detail in Section 2.5. For each spectrum we mask emission-line regions of the quasar, fit the line-free regions with low-order polynomials plus a flux re-scaled unresolved quasar template, and then fit the narrow emission lines with Gaussian functions. The spatial distribution of the flux re-scaling factors of the unresolved quasar template forms a model for the point-spread function. The low-order polynomials account for imperfections in calibrations, including instrumental scattered light subtraction, sky subtraction, foreground source subtractions, and modelling the quasar point-spread function. To demonstrate that processing with CWITools and IFSFIT reduces calibration imperfections and removes foreground objects, in Fig. 2 we show spectrally integrated, white-light images obtained from collapsing the data cube before and after subtracting a median filter to the background field, foreground sources, and low-order polynomials in wavelength space. We fit a circular Moffat function to the empirical point-spread function and find a FWHM of 1.4 arcsec. The size of this point-spread function is slightly larger than the atmospheric seeing disc, which may be attributed to the mosaicking procedure and variable seeing. We correct all measurements of surface brightnesses, spatially-integrated fluxes, and luminosities for a Galactic extinction of  $A_V = 0.214$  (Schlafly & Finkbeiner 2011) toward the quasar location. This corresponds to a 33 per cent upward correction at  $\text{Ly}\alpha$ , a 24 per cent upward correction at  $\text{C IV } \lambda 1549$ , and a 22 per cent upward correction at  $\text{He II } \lambda 1640$ .

## 2.5 Isolating Narrow Emissions in the Central 1-arcsec

In rest-frame UV spectra of blue unobscured quasars, the narrow emission lines that originate far from the quasar broad-line regions are much weaker than the broad emission lines and smoothly blend with them. Generally the spatially-unresolved quasar spectral template is generated by simply summing a circular aperture matching the size of the seeing disc and centred on the quasar, as the narrow and broad emission lines cannot be easily separated. For this study of an ERQ, the broad-line region is partially obscured so that narrow lines can be identified as kinematically distinct components. To make the unresolved quasar template we subtract the narrow emission lines. Fig. 3 displays spectra of summing 1-arcsec, 2-arcsec, 3-arcsec, and 4-arcsec circular apertures centred on the quasar in the data cube, all scaled to match the continuum level of the 2-arcsec aperture spectrum. The Earth atmosphere’s glow at  $[\text{O I}] \lambda 5577$  is omitted from all spectra. With increasing aperture sizes, the flux level of the broad emission in  $\text{Ly}\alpha$ ,  $\text{N V } \lambda 1240$ ,  $\text{Si IV } \lambda 1398$ , and  $\text{C IV } \lambda 1549$  relative to the continuum remains unchanged. This confirms that the broad-line region is spatially unresolved, and should be part of the quasar template. On the contrary, the flux level of the prominent  $\text{Ly}\alpha$  emission spike increases with aperture size. This indicates the narrow

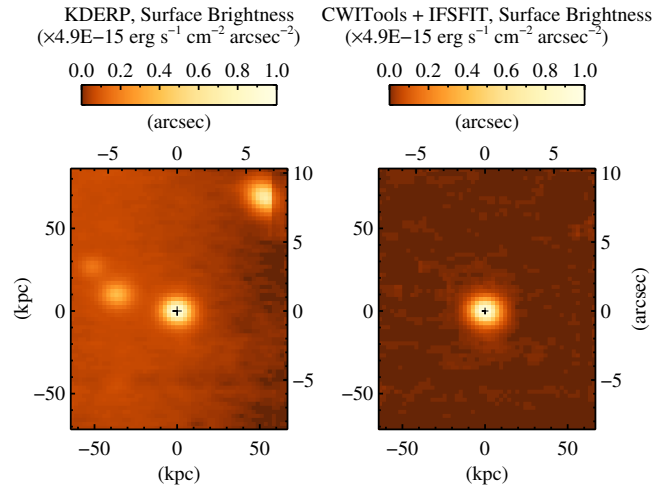


**Figure 2.** The left panel shows a white-light image obtained from the reduced, mosaicked, spatially resampled data cube output by KDERP and IFSRED. The right panel shows a white-light image obtained from the further processed data cube that have residual background light and foreground sources subtracted using CWITools and IFSFIT. The cross symbol marks the peak of the quasar. Comparing the two images, residual background coming from imperfect calibrations is reduced and foreground objects are removed.

$\text{Ly}\alpha$ -emitting region is not part of the spatially unresolved point-spread function. To make the quasar template, we clip the  $\text{Ly}\alpha$  spike, and fit and subtract any narrow emission in  $\text{C IV } \lambda 1548, 1550$  and  $\text{He II } \lambda 1640$  from a spectrum extracted from a circular aperture of 1 arcsec diameter. The aperture size is determined as a compromise between including enough of the quasar’s emission for good signal-to-noise (S/N) while also minimizing spatially extended emission.

We construct the unresolved quasar spectral template by extracting a one-dimensional spectrum from a 1-arcsec aperture centred on the quasar and subtracting narrow line emissions. Fig. 4 shows zoom-ins of the  $\text{Ly}\alpha$  region, the  $\text{C IV } \lambda 1549$  region, and the  $\text{He II } \lambda 1640$  region of this spectrum. Overplotted on the data is our fits. We use the  $\text{Ly}\alpha$  spike to determine the systemic redshift of the quasar host galaxy and we describe our fitting of the spike below. As shown in Fig. 3, the broad  $\text{Ly}\alpha$ - $\text{N V } \lambda 1240$  emission complex underlying the spike in a local wavelength range appears linear in shape. We fit a single Gaussian component to the narrow  $\text{Ly}\alpha$  emission plus a linear function to the part of the broad  $\text{Ly}\alpha$ - $\text{N V } \lambda 1240$  complex underlying it. The blue side of the narrow  $\text{Ly}\alpha$  line profile has an absorption feature, and is masked in the fitting process. The evidence for the blue side absorption is verified in the analysis of the  $\text{Ly}\alpha$  halo spectrum which is discussed in Section 3.4. We find  $z_{\text{sys}, \text{Ly}\alpha} = 2.3184$  from the Gaussian component of the fit, and we adopt this systemic redshift for all relative velocity measurements. We do not attempt to fit the full  $\text{Ly}\alpha$ - $\text{N V } \lambda 1240$  complex.

Fig. 4 shows that at the systemic velocity defined by the narrow  $\text{Ly}\alpha$ , the  $\text{C IV } \lambda 1549$  profile has a shoulder-like feature and the  $\text{He II } \lambda 1640$  profile has a narrow emission feature. The coincidence between the peak of  $\text{Ly}\alpha$  and that of the non-resonant  $\text{He II } \lambda 1640$  suggests that the absorption on  $\text{Ly}\alpha$  is not strong, and the emission at zero velocity is not absorbed. This supports our assertion that the peak of  $\text{Ly}\alpha$  is a good tracer of the systemic velocity. As narrow lines’ contribution to the total  $\text{C IV } \lambda 1549$  profile is weaker and is a blended doublet, we cannot assess whether the absorption feature in the narrow  $\text{Ly}\alpha$  is present in  $\text{C IV } \lambda 1549$ . To measure and remove the



narrow line contributions in C IV  $\lambda$ 1549 and He II  $\lambda$ 1640 we need to estimate the broad-line profiles near them, although our goal is not to extract the broad lines. We speculate that the narrow emission lines all arise on spatial scales much further out than the quasar broad-line region. We discuss evidence supporting this in Section 3.4.

We fit a single power law to line-free regions. This continuum fit is subtracted from the data when analyzing the line emissions.

The C IV  $\lambda$ 1549 emission profile is broad and asymmetric. This emission is a doublet. In the panel for C IV  $\lambda$ 1549 in Fig. 4, velocities are defined relative to the average of the rest wavelengths of the doublet, 1549.48 Å. The doublet separation of C IV  $\lambda$ 1548,1550 at 498 km s<sup>-1</sup> is much smaller than the velocity width of the broad component of one line of this doublet, but is comparable to the velocity width of the narrow component of one line of this doublet. The shoulder-like feature is on the red side of the emission profile. A single Gaussian function can capture the shape of the red side of the broad component of the total blended doublet, while two Gaussians are necessary to capture the shape of the narrow component of the total blended doublet. We thus fit the C IV  $\lambda$ 1549 region with a broad Gaussian function plus two narrow Gaussian functions. The two narrow Gaussian functions are fixed at the doublet separation, and represent a C IV  $\lambda$ 1548,1550 doublet whose velocity centroids and widths are fixed at the narrow Ly $\alpha$ 's values. With respect to the average rest wavelength of the doublet, i.e. zero velocity is midway between the doublet lines, on Fig. 4 the two narrow Gaussians at zero velocity with respect to the systemic are placed at -249 km s<sup>-1</sup> and +249 km s<sup>-1</sup>. During the fitting process we mask the asymmetric blue side.

The He II  $\lambda$ 1640 emission is broad and asymmetric. The narrow component is on the red side of this line profile. We fit with a broad Gaussian function plus a narrow Gaussian function. We fix the narrow Gaussian's velocity centroid and width at the narrow Ly $\alpha$ 's values. During the fitting we mask the asymmetric blue side.

As illustrated in Fig. 4, the narrow emission in all of Ly $\alpha$ , C IV  $\lambda$ 1548,1550, and He II  $\lambda$ 1640 is well fitted with a single component. All three narrow emission lines have similar kinematics. The results of the above line fitting processes are reported in Table 1. We present formal  $\chi^2$  errors on parameters that are free during the fitting, and we note that the formal  $\chi^2$  values may underestimate the true uncertainties due to degeneracies in the parameters. In the same table we also present fitting results on the spatially-integrated, halo-scale emissions that are described in Section 3.4.1.

### 3 ANALYSIS AND RESULTS

#### 3.1 Quasar Spectral Properties

A BOSS spectrum of the quasar was obtained on 2011 December 17, with a fibre aperture of 2-arcsec diameter. A 2-arcsec aperture spectrum extracted from the KCWI data has similar spectral resolution but much higher S/N than BOSS. The higher S/N reveals for the first time the presence of narrow emission components in C IV  $\lambda$ 1548,1550 and He II  $\lambda$ 1640, which have similar kinematics as the Ly $\alpha$  spike that was already clearly present in the BOSS spectrum, as shown in Fig. 1. The broad emission lines are spatially unresolved, hence we may compare emission line properties of a central 1-arcsec spectrum extracted from KCWI data to the BOSS spectrum. These observations taken two years apart in quasar's frame also provide a test for variability.

The  $z_{\text{sys,Ly}\alpha} = 2.3184$  we find from the Ly $\alpha$  spike is very similar to the  $z_{\text{sys,[OIII]}} = 2.3198$  measured by Perrotta et al. (2019) from the

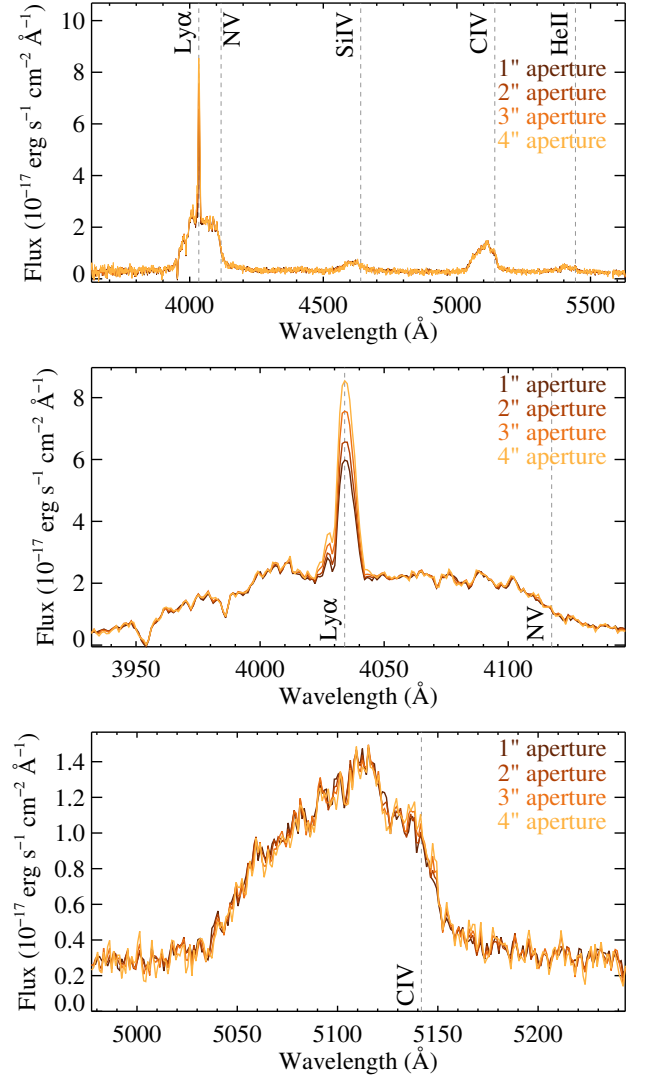


**Figure 3.** The panels show spectra extracted from circular apertures of 1 arcsec, 2 arcsec, 3 arcsec, and 4 arcsec in diameter and centred on the quasar, all scaled to the continuum level of the 2-arcsec spectrum. In the top panel the full spectra are shown. The prominent spike is Ly $\alpha$  emission, which defines the systemic frame. Locations of N v  $\lambda$ 1240, Si iv  $\lambda$ 1398, C iv  $\lambda$ 1549, and He II  $\lambda$ 1640 in this frame are marked with vertical dashed lines. With increasing aperture sizes, the flux level of the broad emission lines relative to the continuum stays unchanged, indicating the broad-line region is spatially unresolved. The middle panel shows a zoom-in of the Ly $\alpha$ -N v region. The flux level of the narrow Ly $\alpha$  increases with aperture size, indicating its emission region is spatially extended. The bottom panel shows a zoom-in of the C iv  $\lambda$ 1548,1550 region. Extended narrow line emissions are not very apparent in C iv and He II  $\lambda$ 1640 and their presence is found by modelling.

narrow component in the [O III]  $\lambda$ 4959,5007 emission lines. The two systemic redshift values are consistent with each other and within one spectral resolution element  $\approx 150$  km s<sup>-1</sup>. The velocity width of the narrow Ly $\alpha$ ,  $\sigma_{\text{Ly}\alpha} = 253$  km s<sup>-1</sup> is also similar to the velocity width of the narrow [O III]  $\lambda$ 4959,5007,  $\sigma_{[\text{OIII}]} = 307$  km s<sup>-1</sup>, implying a possible origin in the same spatial region.

Our measurements made on the central 1-arcsec KCWI spectrum are reported in Table 2. We measure the total blended doublet Si iv  $\lambda$ 1398, the total and the broad component of the blended

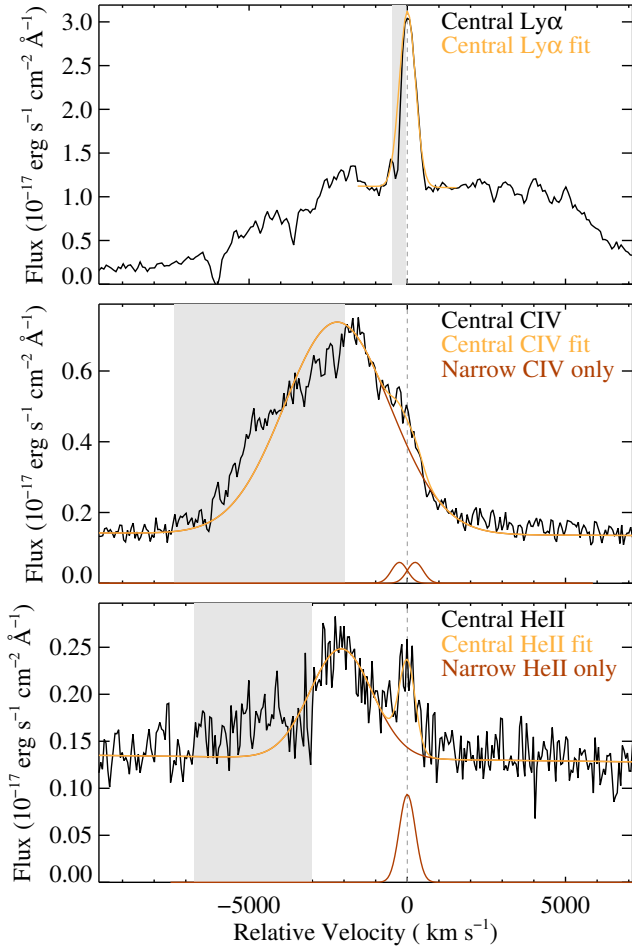


**Figure 4.** Fitting for the narrow component of emission lines in the central 1-arcsec aperture. The black curves are the data, the orange curves are the fits, and the grey shades are regions masked during fitting. Grey dashed lines mark locations of zero velocities. Top panel shows the Ly $\alpha$  region. The fit is the sum of a Gaussian plus a linear function. The absorption on the blue side of the line profile is masked. The peak of this fit is adopted as the systemic velocity. Middle panel shows the C IV  $\lambda$ 1549 region. The fit is the sum of a broad Gaussian, two narrow Gaussians of fixed separation, plus a continuum. The asymmetric blue side of the line is masked, and the kinematics of the narrow component of the C IV  $\lambda$ 1548,1550 doublet are fixed at narrow Ly $\alpha$ 's. The brown curve separately plots the sum of the broad Gaussian plus the continuum and the sum of the two narrow Gaussians. Bottom panel shows the He II  $\lambda$ 1640 region. The fit is the sum of a broad Gaussian, a narrow Gaussian, plus a continuum. The blue side of the line is masked, and the narrow component's kinematics are fixed at narrow Ly $\alpha$ 's. The brown curve separately plots the sum of the broad Gaussian plus the continuum and the narrow Gaussian.

doublet C IV  $\lambda$ 1549, and the total and the broad component of the singlet He II  $\lambda$ 1640. We isolate the broad components by subtracting the narrow emission line fits from the data. For the total Si IV  $\lambda$ 1398 emission, the total C IV  $\lambda$ 1549 emission, and the broad component of C IV  $\lambda$ 1549, we report the velocity centroid, FWHM velocity, the kurtosis index  $kt_{80}$ , and the rest equivalent width values. As the total C IV  $\lambda$ 1549 line profile is dominated by the broad component, the measurements on the broad component are very similar to the measurements on the total line profile. The total He II  $\lambda$ 1640 emission is weak and has contribution from narrow emission that is comparable

**Table 1.** Results of Gaussian Fitting the Narrow Emissions in the Central 1-arcsec and the Spatially-Integrated Halo Emissions

Line Component	Flux ( $\text{erg s}^{-1} \text{cm}^{-2}$ )	Centre <sup>a</sup> ( $\text{km s}^{-1}$ )	$1\sigma$ Dispersion ( $\text{km s}^{-1}$ )
Narrow Emissions in Central Spectrum			
H I Ly $\alpha$	$(1.72 \pm 0.05) \times 10^{-16}$	$0 \pm 8$	$253 \pm 5$
C IV $\lambda$ 1548	$(6.4 \pm 0.9) \times 10^{-18}$	0	253
C IV $\lambda$ 1550 <sup>b</sup>	$6.4 \times 10^{-18}$	0	253
He II $\lambda$ 1640	$(1.1 \pm 0.1) \times 10^{-17}$	0	253
Spatially-Integrated Halo Emissions			
H I Ly $\alpha$	$(1.45 \pm 0.01) \times 10^{-15}$	$-46 \pm 3$	$304 \pm 2$
C IV $\lambda$ 1548	$(3.41 \pm 0.07) \times 10^{-17}$	$-44 \pm 3$	$319 \pm 4$
C IV $\lambda$ 1550 <sup>b</sup>	$3.41 \times 10^{-17}$	-44	319
He II $\lambda$ 1640	$(1.78 \pm 0.07) \times 10^{-17}$	$-45 \pm 7$	$238 \pm 7$

<sup>a</sup>The narrow Ly $\alpha$  line centre in the central spectrum is defined to be the zero velocity. Other lines in the central spectrum are forced to be at zero velocity.

<sup>b</sup>C IV  $\lambda$ 1550 is locked to C IV  $\lambda$ 1548.

to the broad emission. We do not attempt to quantify the kurtosis of the total He II  $\lambda$ 1640 or the broad component of He II  $\lambda$ 1640. The  $kt_{80}$  quantity characterizes line profile shapes and measures the velocity width at 80 per cent of the peak height divided by the width at 20 per cent. For reference, a single Gaussian function has  $kt_{80} = 0.372$  while most quasars have substantial line wings yielding lower values 0.15–0.3.

Our measurements on the total C IV  $\lambda$ 1549 profile in the central 1-arcsec KCWI spectrum are similar to the measurements by Hamann et al. (2017) on the BOSS spectrum. They report a blueshift of  $2267 \text{ km s}^{-1}$  estimated from the profile centre at half maximum relative to the Ly $\alpha$  spike, a rest equivalent width of  $107 \pm 6 \text{ \AA}$ , a FWHM velocity of  $4540 \pm 200 \text{ km s}^{-1}$ , and a  $kt_{80}$  of 0.37. Small differences between these measurements and Table 2 may be due to quasar variability or differences in measurement techniques. The broad Ly $\alpha$ -N V  $\lambda$ 1240 complex has decreased in strength since BOSS, although we do not attempt to measure the rest equivalent widths of these heavily blended lines. The overall similarity between the two sets of measurements indicates that the peculiar spectral properties of this ERQ persisted over this period of two years in the quasar rest frame, consistent with the repeat observations of other ERQs in Hamann et al. (2017).

## 3.2 Morphology and Brightness of the Extended Line Emissions

### 3.2.1 Optimal Extraction of Diffuse Emissions

Relative to standard pseudo-narrowband images, an optimal extraction algorithm better captures the morphology and kinematic features of diffuse extended line emissions. We optimally extract extended line emissions, if any, in the H I Ly $\alpha$ , C IV  $\lambda$ 1549, and He II  $\lambda$ 1640, follow an algorithm similar to that described in Borisova et al. (2016), Arrigoni Battaia et al. (2019), Cai et al. (2019), and Farina et al. (2019). We subtract the quasar point spread function constructed using the unresolved quasar spectral template. We only use portions of the cube within  $\pm 5000 \text{ km s}^{-1}$  around the line wavelengths at the systemic redshift. This relative velocity range corresponds to  $\sim 150 \text{ \AA}$  in observer's frame. Each wavelength layer of the data cube and the

**Table 2. Quasar Emission Line Properties in the Central 1 arcsec**

Line Component	Centroid <sup>a</sup> (km s <sup>-1</sup> )	FWHM (km s <sup>-1</sup> )	$kt_{80}$ <sup>b</sup>	REW <sup>c</sup> (Å)
Total Si IV $\lambda$ 1398	-1770 $\pm$ 180	4750 $\pm$ 280	0.37 $\pm$ 0.02	30 $\pm$ 1
Total C IV $\lambda$ 1549	-2180 $\pm$ 50	5110 $\pm$ 60	0.30 $\pm$ 0.01	102 $\pm$ 1
Broad C IV $\lambda$ 1549 <sup>d</sup>	-2240 $\pm$ 50	4880 $\pm$ 70	0.31 $\pm$ 0.01	99 $\pm$ 1
Total He II $\lambda$ 1640	-2110 $\pm$ 250	3431 $\pm$ 120	–	19 $\pm$ 1
Broad He II $\lambda$ 1640 <sup>d</sup>	-2430 $\pm$ 300	2330 $\pm$ 140	–	16 $\pm$ 1

<sup>a</sup>Centroid of the line or doublet in velocity relative to the systemic redshift.

<sup>b</sup>Kurtosis index  $kt_{80}$  of the line or doublet.

<sup>c</sup>Equivalent width of the line or doublet in rest-frame wavelength.

<sup>d</sup>The broad component is obtained from subtracting the narrow emission line fits from the data.

variance cube is smoothed with a two-dimensional Gaussian kernel of  $\sigma_{\text{spatial}} = 0.4$  arcsec. The FWHM of the chosen kernel, 0.9 arcsec, matches the seeing disc and is conservative compared to the size of the point spread function measured on the data. The smoothing in spatial dimensions without smoothing in wavelength helps reveal extended and narrow features. We then create a three-dimensional segmentation mask that selects connected voxels (volume pixels) around a given line wavelength that are of S/N > 2 and in groups of minimal 200 voxels. In three dimensions, connected voxels are neighbours to every voxel that touches one of their faces, edges, or corners. The minimum number of connected voxels is empirically derived to avoid selecting instrument artifacts that are not fully removed in data reduction and post-processing. For each of the Ly $\alpha$ , C IV  $\lambda$ 1549, and He II  $\lambda$ 1640, an optimally extracted image is constructed by summing the flux along the wavelength direction for only the voxels selected by the line's three-dimensional segmentation mask.

### 3.2.2 Morphology and Brightness Measurements

In Fig. 5 we show the optimally extracted images of the Ly $\alpha$ , C IV  $\lambda$ 1549, and He II  $\lambda$ 1640 line emissions down to a S/N threshold of two, corresponding to a surface brightness limit  $\approx 3 \times 10^{-19}$  erg s<sup>-1</sup> cm<sup>-2</sup> arcsec<sup>-2</sup>. The spatially-integrated luminosities, maximum linear sizes, and areas covered by the line emissions are tabulated in Table 3. The Ly $\alpha$  and C IV  $\lambda$ 1549 line emissions are clearly spatially extended, and their maximum linear sizes within covered areas of S/N > 2 are respectively 140 kpc and 47 kpc. The He II  $\lambda$ 1640 emission is marginally spatially resolved with a maximum linear size of 33 kpc, and the majority of the line flux is contained within the FWHM of the point spread function that is 1.4 arcsec or 12 kpc.

We define an inner halo region  $\sim(20\text{--}30)$  kpc from the centre and an outer halo region beyond. This definition is motivated by the morphology analysis, the line ratio analysis, and the kinematics analysis in this and the next two subsections, where we find that measured properties transition near these distances. Evidence that gaseous halo properties transition near similar scales has been reported in the literature and is discussed in Section 4.2.

We quantify the spatial asymmetry of the flux distributions in the optimally extracted images as follows. For each line, we calculate the halo centroid as the first spatial moment of the line flux within areas of S/N > 2. We then measure the projected distance between the quasar and the peak of the line emission, and the projected distance between the quasar and the centroid. We then calculate two dimen-

sionless parameters measuring circular asymmetry that respectively emphasize the brighter inner halo region and the overall diffuse halo emission. These quantities are tabulated in Table 3.

The uncertainty in the projected distance between the quasar and an extended line emission's peak or centroid is estimated to be about half a spaxel's size, or  $\approx 1$  kpc in physical distance. The peaks of Ly $\alpha$  and C IV  $\lambda$ 1549 are spatially offset from the position of the quasar by similar amounts of 3 kpc and in similar general directions. The centroids of Ly $\alpha$  and C IV  $\lambda$ 1549 are spatially offset from the position of the quasar by similar amounts of 5 kpc and in similar general directions. The extended emission in all three lines have their peaks and centroids in close proximity of the quasar, indicating only a low level of asymmetry in the inner halo. The position of the Ly $\alpha$  halo centroid is used in assessing spatial asymmetry in this section and the position of the Ly $\alpha$  halo peak is used in analysis of aperture kinematics in Section 3.4.2.

We define an elliptical eccentricity parameter  $e_{\text{weight}}$  using flux-weighted second-order spatial moments with respect to the halo centroid according to the formulae in O'Sullivan & Chen (2020). This parameter reflects the ratio of the semiminor axis to the semimajor axis of the extended line emission. A value of  $e \ll 1$  indicates very circular morphology, while  $e \approx 1$  indicates very asymmetric shape. The definition of  $e_{\text{weight}}$  tends to weight toward asymmetries on smaller scales and with respect to where most of the halo emission is. This  $e_{\text{weight}}$  parameter is related to the flux-weighted asymmetry parameter  $\alpha$  defined in Arrigoni Battaia et al. (2019) or Cai et al. (2019) by  $e_{\text{weight}} = \sqrt{1 - \alpha_{\text{weight}}^2}$ . We define another elliptical eccentricity parameter  $e_{\text{unweight}}$  using flux-unweighted second-order spatial moment with respect to the quasar position. The definition of  $e_{\text{unweight}}$  better characterizes asymmetries on larger scales and with respect to the powering source, the quasar. This  $e_{\text{unweight}}$  parameter is related to the flux-unweighted asymmetry parameter  $\alpha$  defined in den Brok et al. (2020) or Mackenzie et al. (2021) by  $e_{\text{unweight}} = \sqrt{1 - \alpha_{\text{unweight}}^2}$ . For the optimally extracted Ly $\alpha$  halo, we find  $e_{\text{weight}} = 0.44$  and  $e_{\text{unweight}} = 0.69$ . The relatively low value of  $e_{\text{weight}}$  indicates that the halo is circularly symmetric in regions where most of the line flux is contained. Indeed, the halo appears symmetric in the inner region on scales  $\lesssim 30$  kpc from the centroid. With a relatively low value of  $e_{\text{weight}}$ , the higher value of  $e_{\text{unweight}}$  indicates some level of asymmetry on larger scales. This large-scale asymmetry characterizes the filamentary appearance of the halo in the outer region on  $\gtrsim 30$  kpc scales.

The Ly $\alpha$  and C IV  $\lambda$ 1549 emissions are spatially extended enough to warrant examination of their radial profiles. While optimally extracted line images better capture the morphology and kinematic features, for the purpose of calculating surface brightness radial profiles we use fixed width pseudo-narrowband images sliced from the quasar-subtracted, unsmoothed data cube. The choice of a fixed width pseudo-narrowband recovers all possible fluxes in extended regions, allows uniform comparison of detections and non-detections, and matches the methods in literature works for comparison. The widths of the Ly $\alpha$  narrowband and the C IV  $\lambda$ 1549 narrowband are set at  $\pm 1000$  km s<sup>-1</sup> from the line rest wavelengths. We sum these two slices of the cube in the spectral dimension. We then bin the pseudo-narrowband images in concentric annuli that are centred on the quasar's position and have bin widths uniformly spaced in a logarithmic scale. Then in each annular bin we circularly average the surface brightness. For comparison with profiles of other line-emitting haloes in the literature at different redshifts, we multiply all surface brightness values by their cosmological dimming factor  $(1+z)^4$ . For each annular bin, we calculate surface brightness limit

under the assumption that there are no unaccounted residuals from the sky, scattered light, continuum sources, or imperfect calibrations, or unaccounted covariances among spaxels. We sum the respective slice of the variance cube in the spectral dimension. We then sum the spaxels belonging to that annular aperture, take the square root, and divide by the angular area of that annulus. The expected surface brightness limit of an annular bin thus scales with the inverse square root of the annular aperture area.

Fig. 6 shows the surface brightness radial profiles and the  $2\sigma$  surface brightness limit profiles of Ly $\alpha$  and C IV  $\lambda$ 1549. Table 4 presents the data of these profiles. We find that the surface brightness radial profiles are better described by exponential laws than power laws. To each of Ly $\alpha$  and C IV  $\lambda$ 1549 we fit the function  $\text{SB}_{\text{Ly}\alpha}(r) = C_e \exp(-r/r_h)$ , where  $C_e$  is the normalization,  $r$  is the projected distance from the quasar, and  $r_h$  is the scale length. The fits are shown in Fig. 6. The resulting parameters for Ly $\alpha$  are  $C_e = (2.46 \pm 0.04) \times 10^{-14} \text{ erg s}^{-1} \text{ cm}^{-2} \text{ arcsec}^{-2}$  and  $r_h = (8.5 \pm 0.1) \text{ kpc}$ , which describe a centrally concentrated profile. The resulting parameters for C IV  $\lambda$ 1549 are  $C_e = (2.0 \pm 0.2) \times 10^{-15} \text{ erg s}^{-1} \text{ cm}^{-2} \text{ arcsec}^{-2}$  and  $r_h = (8.2 \pm 0.7) \text{ kpc}$ .

### 3.3 Line Ratios in the Extended Emissions

We construct maps of surface brightness ratios from the optimally extracted line images of H I Ly $\alpha$ , C IV  $\lambda$ 1549, and He II  $\lambda$ 1640. We compute the ratios only in regions where both lines in a ratio are detected at  $S/N > 2$ . These regions are out to  $\sim 20 \text{ kpc}$  from the quasar for C IV  $\lambda$ 1549/Ly $\alpha$  and out to  $\sim 10 \text{ kpc}$  from the quasar for He II  $\lambda$ 1640/Ly $\alpha$ . Fig. 7 shows maps of C IV  $\lambda$ 1549/Ly $\alpha$  and He II  $\lambda$ 1640/Ly $\alpha$ . Table 5 presents the ratios of line fluxes spatially integrated over regions of significant detection. The same ratios may be measured from the extracted narrow line emissions from the 1-arcsec aperture spectrum centred on the quasar, and they are also presented in Table 5.

The central 1-arcsec C IV  $\lambda$ 1549/He II  $\lambda$ 1640 ratio is of order unity, while the spatially-integrated ratio shows the C IV  $\lambda$ 1549 brightness is somewhat higher than He II  $\lambda$ 1640. Quasar photoionization models predict C IV  $\lambda$ 1549 and He II  $\lambda$ 1640 brightnesses of the same order for the ranges of metallicities and gas densities in circumgalactic environments (Feltre et al. 2016; Humphrey et al. 2019). The observed line ratios are consistent with quasar photoionization being the major powering mechanism of the extended line emissions.

Both C IV  $\lambda$ 1549/Ly $\alpha$  and He II  $\lambda$ 1640/Ly $\alpha$  ratios decline outwardly. This reflects a steeper radial decline in C IV  $\lambda$ 1549 brightness and He II  $\lambda$ 1640 brightness than Ly $\alpha$ . The spatially-integrated values of C IV  $\lambda$ 1549/Ly $\alpha$  and He II  $\lambda$ 1640/Ly $\alpha$  are lower than the central 1-arcsec line ratios, again reflecting the outward declines. The outward decline of these line ratios reflects a decline of the ionization parameter with distance from the ionizing source (Feltre et al. 2016; Humphrey et al. 2019), which holds for a density gradient less steep than inverse distance squared.

The He II  $\lambda$ 1640/Ly $\alpha$  ratios at all significantly detected spaxels are much lower than the theoretical limits for Case A or Case B recombination in a fully photoionized gas, which are respectively 0.23 and 0.3 (Cantalupo et al. 2019). This suggests that helium is not fully doubly ionized, and the amount of He II  $\lambda$ 1640 emission by fluorescent recombination is ionization-bounded.

Knowledge of both C IV  $\lambda$ 1549/He II  $\lambda$ 1640 and C III]  $\lambda$ 1909/C IV  $\lambda$ 1549 would have provided diagnostics for the ionization levels and the metallicities of the emitting gas, given quasar photoionization models. Our data do not cover C III]  $\lambda$ 1909, and the C IV  $\lambda$ 1549/He II  $\lambda$ 1640 ratio alone does not provide mean-

ingful simultaneous constraints to the ionization parameter and the metallicity. In Guo et al. (2020) which study the average extended line emissions around  $z \sim 3$  luminous blue quasars, metallicities of circumgalactic gas at different ionization parameters are given on a line ratio diagnostic diagram. We may make the assumption that the ionization parameter  $U$  of the inner halo region of J0006+1215 where both C IV  $\lambda$ 1549 and He II  $\lambda$ 1640 are detected is similar to that of Guo et al. (2020). With this assumption, at  $\log U \sim -1$  the central 1-arcsec C IV  $\lambda$ 1549/He II  $\lambda$ 1640 ratio of  $\sim 1$  corresponds to a metallicity  $\sim 1 Z_\odot$ , and the spatially-integrated line ratio of  $\sim 3$  corresponds to a metallicity  $\sim 0.5 Z_\odot$ . This inner halo enrichment level is similar to the stacked inner halo of Guo et al. (2020). The high enrichment level suggests centrally-driven outflow events of gas processed by multiple stellar generations and the outflows deposit materials out to at least  $\sim (20\text{--}30) \text{ kpc}$  from the host galaxy.

### 3.4 Kinematics of the Extended Line Emissions

We characterize the overall halo kinematics using spatially integrated and spatially resolved spectra. A baseline comparison for assessing the velocity fields would be the circular velocity of the host dark matter halo. J0006+1215 is selected from BOSS quasars. From clustering measurements of BOSS quasars at similar redshifts, the average host dark matter halo mass is  $10^{12.4} h^{-1} M_\odot$  (Eftekharzadeh et al. 2015). At this dark matter halo mass and J0006+1215's redshift, and assuming a halo concentration parameter of 4, the maximum circular velocity is  $v_{\text{circ}} = 338 \text{ km s}^{-1}$ . From analytical arguments that are verified by numerical simulation results, the one-dimensional velocity dispersion is related to the circular velocity by  $v_{\text{circ}} \approx \sqrt{2} \sigma_{\text{1D}}$  (Binney & Tremaine 2008; Lau et al. 2010; Munari et al. 2013). The corresponding  $\sigma_{\text{1D}}$  is thus  $239 \text{ km s}^{-1}$ . On the other hand, J0006+1215 has among the highest bolometric luminosities of BOSS quasars. Evidence has been found that obscured quasars and hyperluminous quasars on average reside in even more massive dark matter haloes typically  $10^{13} h^{-1} M_\odot$  (DiPompeo et al. 2017; Geach et al. 2019). At this dark matter halo mass  $v_{\text{circ}} = 536 \text{ km s}^{-1}$  and  $\sigma_{\text{1D}} = 379 \text{ km s}^{-1}$ . Halo gas with measured line-of-sight speeds much greater than  $379 \text{ km s}^{-1}$  may thus be considered fast moving.

#### 3.4.1 Spatially-Integrated Kinematics

We extract the spatially-integrated spectra of Ly $\alpha$ , C IV  $\lambda$ 1548,1550, and He II  $\lambda$ 1640. For each line or doublet, we select the spaxels for summing using a two-dimensional mask obtained by collapsing the spectral dimension of its three-dimensional segmentation mask. To describe the overall line profiles, we follow the procedure in Section 2.5 and Fig. 4 for fitting the narrow emission lines in the central 1-arcsec spectrum. The spatially-integrated emission-line spectra and our fits are presented in Fig. 8. The resulting velocity centres and Gaussian  $1\sigma$  velocity dispersions of the fits are presented in Table 1.

In Section 2.5, we measure the redshift of the narrow Ly $\alpha$  emission in the central 1-arcsec spectrum and adopt it to be the systemic. The fitted line centres of spatially-integrated Ly $\alpha$ , C IV  $\lambda$ 1548,1550, and He II  $\lambda$ 1640 are within one spectral resolution element from the systemic redshift. The similar line centres and line widths between the spatially-integrated emissions and the central 1-arcsec emissions support our assertion that the narrow emission lines in the central 1-arcsec spectrum originate far from the quasar at halo-scale distances.

Ly $\alpha$  and C IV  $\lambda$ 1548,1550 are resonant lines. Resonant scattering is not efficient for C IV photons, due to the much lower abundance of metals. He II  $\lambda$ 1640 and [O III]  $\lambda$ 5007 are non-resonant. The similar line profiles of Ly $\alpha$ , He II  $\lambda$ 1640, and the narrow component of



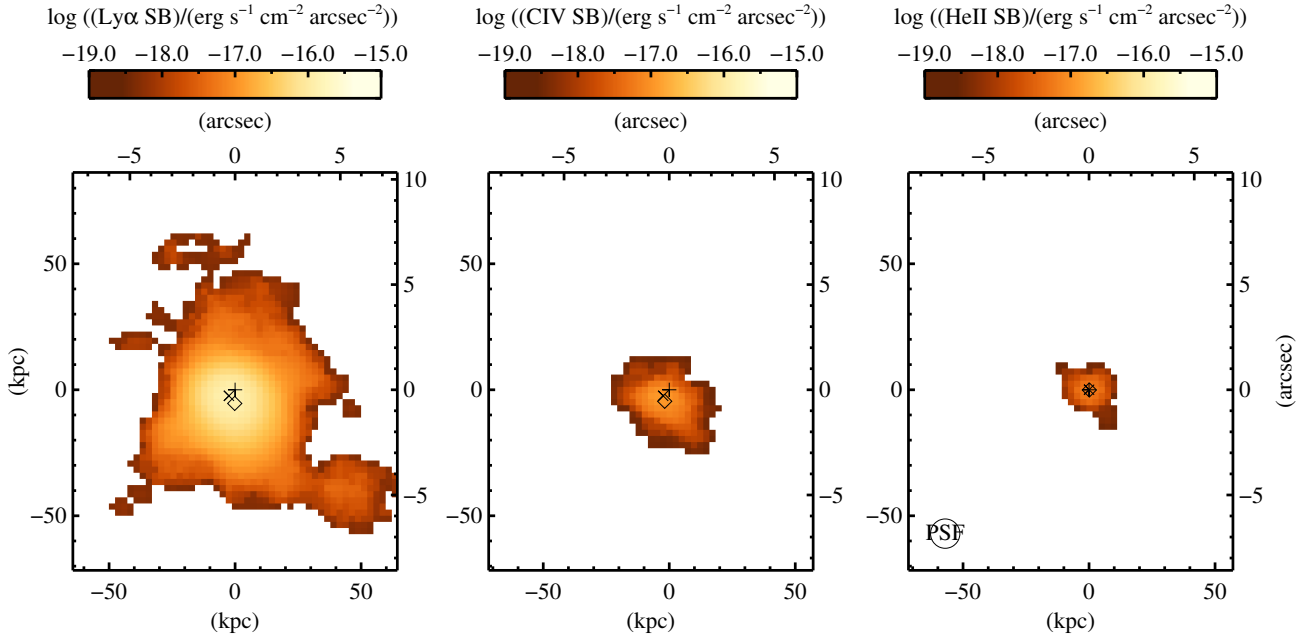


**Figure 5.** Optimally extracted images of Ly $\alpha$ , C IV  $\lambda$ 1549, and He II  $\lambda$ 1640 after subtracting the quasar. On each image the white contours indicate the area detected above a S/N threshold of two. On each image the plus symbol marks the position of the quasar, the cross symbol marks the position of the peak of the extended line emission, and the diamond symbol marks the position of the centroid of the extended line emission. The spatial axes of each image have angular distances transformed to projected proper distances. On the He II  $\lambda$ 1640 image, the FWHM of the empirical point spread function is displayed. On these maps and all subsequent figures of maps, north is pointing upright.

**Table 3.** Size and Morphology Measures of the Extended Line Emissions

Line Name	Area Covered (kpc <sup>2</sup> )	Maximum Linear Size (kpc)	Luminosity (erg s <sup>-1</sup> )	Peak to QSO Distance <sup>a</sup> (kpc)	Centroid to QSO Distance <sup>b</sup> (kpc)	$e_{\text{weight}}^c$	$e_{\text{unweight}}^d$
H I Ly $\alpha$	7005	140	$5.11 \times 10^{43}$	3 $\pm$ 1	5 $\pm$ 1	0.44	0.69
C IV $\lambda$ 1549	1210	47	$1.81 \times 10^{42}$	3 $\pm$ 1	5 $\pm$ 1	0.71	0.64
He II $\lambda$ 1640	437	33	$4.90 \times 10^{41}$	0 $\pm$ 1	0 $\pm$ 1	–	–

<sup>a</sup>Distance between the position of the peak of halo emission and the position of the quasar.

<sup>b</sup>Distance between the position of the centroid of halo emission and the position of the quasar.

<sup>c</sup>Flux-weighted elliptical eccentricity with respect to the halo centroid position  $e_{\text{weight}}$ , calculated from flux-weighted spatial moments.

<sup>d</sup>Unweighted elliptical eccentricity with respect to the quasar position  $e_{\text{unweight}}$ , calculated from unweighted spatial moments.

**Table 4.** Circularly Averaged Surface Brightness Profiles of the Extended Line Emissions

Radii <sup>a</sup> (kpc)	H I Ly $\alpha$ <sup>b</sup>	Ly $\alpha$ 2 $\sigma$ Limit <sup>c</sup> (erg s <sup>-1</sup> cm <sup>-2</sup> arcsec <sup>-2</sup> )	C IV $\lambda$ 1549 <sup>b</sup>	C IV 2 $\sigma$ Limit <sup>c</sup>
2–4	$(1708.6 \pm 35.1) \times 10^{-17}$	$45.6 \times 10^{-17}$	$(137.7 \pm 18.4) \times 10^{-17}$	$29.6 \times 10^{-17}$
4–8	$(1264.9 \pm 16.6) \times 10^{-17}$	$24.4 \times 10^{-17}$	$(98.1 \pm 9.1) \times 10^{-17}$	$15.8 \times 10^{-17}$
8–16	$(597.0 \pm 7.4) \times 10^{-17}$	$12.9 \times 10^{-17}$	$(47.2 \pm 4.4) \times 10^{-17}$	$8.4 \times 10^{-17}$
16–32	$(150.3 \pm 3.5) \times 10^{-17}$	$6.6 \times 10^{-17}$	$(10.6 \pm 2.2) \times 10^{-17}$	$4.3 \times 10^{-17}$
32–63	$(18.0 \pm 1.7) \times 10^{-17}$	$3.2 \times 10^{-17}$	$(1.3 \pm 1.1) \times 10^{-17}$	$2.1 \times 10^{-17}$

<sup>a</sup>Radii spanned by the annular bins.

<sup>b</sup>Corrected for cosmological dimming.

<sup>c</sup>Expected 2 $\sigma$  surface brightness limit in the aperture, under the assumptions of perfect calibrations and other processings of the data.

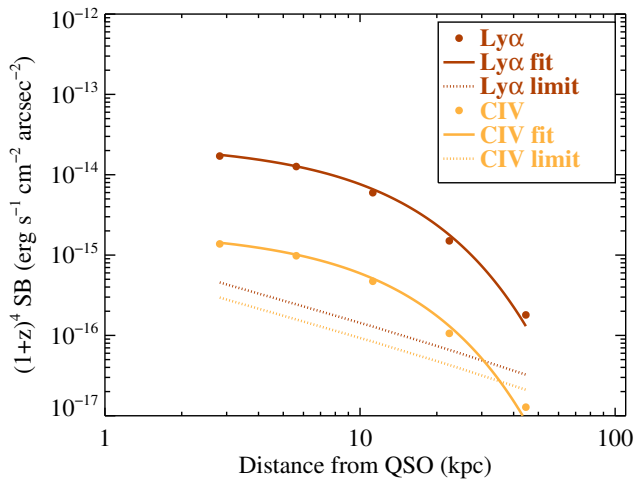


**Figure 6.** Circularly averaged surface brightness radial profiles of Ly $\alpha$  and C IV  $\lambda$ 1549, created from their pseudo-narrowband images. Bins of surface brightness are measured in concentric annuli centred on the quasar, and the bin widths are uniformly spaced on a logarithmic scale. Brown colours show Ly $\alpha$  and orange colours show C IV  $\lambda$ 1549. The points are the measured data. The solid curves are exponential function fits to the data points. The dotted lines are the pseudo-narrowband  $2\sigma$  surface brightness limits in the annular apertures. All surface brightnesses are corrected for cosmological dimming.

**Table 5.** Summary of Line Ratios in the Extended Emission

Lines	Inner Halo <sup>a</sup>	Central 1 arcsec <sup>b</sup>
(C IV $\lambda$ 1549)/(H I Ly $\alpha$ )	0.04	0.07
(He II $\lambda$ 1640)/(H I Ly $\alpha$ )	0.01	0.06
(C IV $\lambda$ 1549)/(He II $\lambda$ 1640)	3.70	1.19

<sup>a</sup>Calculated in regions where both lines in a ratio have S/N > 2.

<sup>b</sup>Calculated using extracted narrow emissions from the central 1 arcsec.

unresolved [O III]  $\lambda$ 5007 published in Perrotta et al. (2019) suggest that scattering of centrally produced Ly $\alpha$  photons is not a major contributor to the observed emission.

The fitted  $1\sigma$  dispersion of spatially-integrated Ly $\alpha$  is somewhat broader than that of the central 1-arcsec narrow Ly $\alpha$ . Likewise the fitted  $1\sigma$  dispersion of spatially-integrated C IV  $\lambda$ 1548,1550 is broader than the extracted narrow C IV  $\lambda$ 1548,1550 emission from the central 1-arcsec spectrum. This is expected as spatial variation of the gas kinematics would broaden the overall line profile. The fitted  $1\sigma$  dispersion of spatially-integrated He II  $\lambda$ 1640 is consistent with that of the extracted narrow He II  $\lambda$ 1640 from the central 1-arcsec spectrum. This is expected as the detectable He II  $\lambda$ 1640 has a small spatial extent that is only marginally larger than the point spread function.

### 3.4.2 Spatially Resolved Kinematics

We create velocity centroid maps obtained as the first moments in velocity space of the flux distribution at each spatial position. To produce these two-dimensional maps we only include significantly detected voxels selected by a line’s three-dimensional segmentation mask. The maps are presented in Fig. 9. Summary statistics of the maps are presented in Table 6.

From the velocity centroid maps, the majority of the line emissions have small shifts relative to the systemic velocity. With the exception of regions associated with low S/N emissions, the velocity shift of detectable C IV  $\lambda$ 1549 and He II  $\lambda$ 1640 are close to the velocity shift measured for Ly $\alpha$  in the same spatial locations, typically within one spectral resolution element. The angular size of the fitted point spread function of the quasar continuum plus broad-line region 1.4 arcsec corresponds to a physical distance of 12 kpc. The velocity fields are thus quiet on scales down to the innermost  $\sim$ 12 kpc in projected linear extent. As the extended Ly $\alpha$  emission has good S/N covering a large area, we may examine its velocity field further. The velocity field is coherent in the inner halo region on scales  $\lesssim$ (20–30) kpc from the halo centroid or the quasar. The halo shows clear velocity shear from the northern edge to the southern edge. The gradient is of an order two times the estimated one-dimensional velocity dispersion of the dark matter halo. Rotating disc of  $\sim$ 100 kpc size is not expected to be in place by  $z \sim 2$  (e.g., DeFelippis et al. 2020; Huscher et al. 2021). Together with the filamentary morphology, the northern and southern edges are most consistent with tracing inflowing streams.

There is not enough signal in the halo to create maps of the second moments in velocity space of the flux distribution (see discussions in O’Sullivan et al. 2020). If only the significantly detected voxels are included in calculating the second moments, wings of the line profiles cannot be captured and the second moment values would be biased low. If all voxels are included, the second moment values would be dominated by noise at large relative velocities. We therefore measure the Ly $\alpha$  velocity dispersion map by fitting Gaussians to a Voronoi-binned map (see Rupke et al. 2019). From Ly $\alpha$  line flux and error maps we construct Voronoi bins with a target S/N of 10 and a threshold S/N of 1. We then fit single Gaussians to the Voronoi-binned data. The Ly $\alpha$  Gaussian velocity dispersion map is presented in Fig. 10 and the summary statistics are presented in Table 6. For the extended C IV  $\lambda$ 1549 or He II  $\lambda$ 1640, there is not enough signal to spatially resolve their velocity dispersions.

From the Ly $\alpha$  velocity dispersion map, the majority of the emission has velocity dispersion comparable to the estimated one-dimensional velocity dispersion of the dark matter halo, typically within 10 per cent. The halo shows some increase in velocity width from the inner region to the outer region. The change is of an order the estimated one-dimensional dark matter velocity dispersion. The velocity dispersion of the Ly $\alpha$  emission is coherent across distant spatial locations, and is consistent with gravitational motions. There is no clear evidence of gravitationally unbound outflows down to half the size of the point spread function  $\sim$ 0.7 arcsec or  $\sim$ 6 kpc scale from the quasar.

Given the velocity shear in the outer Ly $\alpha$  halo and the coherence and quietness in the inner Ly $\alpha$  halo, we define three apertures according to the features on the velocity centroid map and the morphology to further examine the kinematics, as shown in Fig. 11. We delineate an outer halo region and an inner halo region with a circle of radius 23 kpc centred on the halo’s peak. We further divide the outer halo into a southern region and a northern region with a slanted line that follows the transition from negative to positive relative velocities. In Fig. 11 we present the one-dimensional spectra extracted from these apertures, and we overplot the central 1-arcsec aperture spectrum on this figure. We find that the Ly $\alpha$  flux in the central 1 arcsec does not dominate the total Ly $\alpha$  flux in the defined inner halo aperture. The Ly $\alpha$  spike in the central 1-arcsec spectrum has a line profile very similar to the Ly $\alpha$  emission in the inner halo aperture, confirming that the spike originates from the inner halo region. The Ly $\alpha$  line profiles of the central 1-arcsec and inner halo spectra, which carry the same blueshifted absorption feature, resemble those of carefully modeled, spatially resolved Ly $\alpha$  halo spectra in the literature that require the

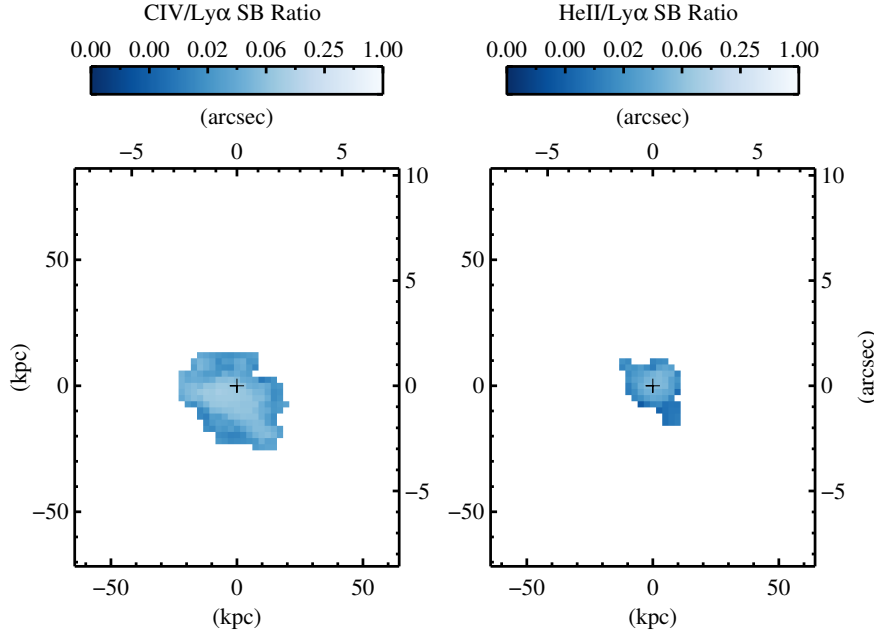


**Figure 7.** Maps of the C IV  $\lambda 1549$ /Ly $\alpha$  line brightness ratio, and the He II  $\lambda 1640$ /Ly $\alpha$  line brightness ratio. The ratio values are calculated only for regions where Ly $\alpha$  and C IV  $\lambda 1549$  are both detected, and regions where Ly $\alpha$  and He II  $\lambda 1640$  are both detected. The plus symbol marks the position of the quasar.

**Table 6.** Summary of Spatially Resolved Velocity Centroids and Dispersions of the Extended Emission

Line Name	Spatial Median (km s <sup>-1</sup> )	Spatial Standard Deviation (km s <sup>-1</sup> )
Velocity Centroid Map		
H I Ly $\alpha$	-85	235
C IV $\lambda 1549$	-23	201
He II $\lambda 1640$	-9	87
Fitted Gaussian Velocity Dispersion Map		
H I Ly $\alpha$	287	70

presence of outflows (e.g., Li et al. 2021). The blueshifted absorption feature is absent in the two outer halo spectra. All three halo aperture spectra show evidence of multiple kinematic components, suggesting that the emitting gas is clumpy.

We identify a narrow absorption feature in the central 1-arcsec spectrum, whose trough relative to the systemic has a velocity of  $-369$  km s<sup>-1</sup>. This absorption feature is spatially coherent across an extent matching the defined inner halo. Assuming that the blueshifted absorption traces a simple isotropic expanding shell-like structure, this value reflects a characteristic outflow speed. While J0006+1215 displays [O III]  $\lambda 5007$  at speeds and velocity widths  $\sim 6000$  km s<sup>-1</sup> emitting at  $\sim 1$  kpc, there is no evidence for this fast flow on halo scales as probed by the KCWI data. For outflows at the measured moderate speeds that are present on scales out to (20–30) kpc, the dynamical time involved will be  $\sim (5\text{--}8)\times 10^7$  yr.

### 3.5 Comparison to Other Quasars

#### 3.5.1 Introducing Comparison Samples and Single Sources

We compare the J0006+1215 line-emitting halo with other samples and single sources from the literature. They are line-emitting haloes surrounding quasars selected by various criteria and are crudely matched in bolometric luminosity and cosmic redshift to J0006+1215, i.e. quasars of  $\geq 10^{46}$  erg s<sup>-1</sup> at cosmic noon. When available we calculate or adopt their halo redshifts, elliptical eccentricity parameters, maximum linear sizes, line luminosities, surface brightness radial profiles, inner halo line ratios, and spatially-integrated velocity dispersions. We estimate all intrinsic bolometric luminosities from W3-band photometries. We apply Galactic extinction corrections to all line luminosities and surface brightnesses. In Table 7 we list the quantities we adopt from these literature samples and single sources. Below are our remarks about them.

The Cai et al. (2019) sample consists of 16 luminous blue quasars of median  $z = 2.3$  and median bolometric luminosity  $10^{47.2}$  erg s<sup>-1</sup>. We adopt their sample median Ly $\alpha$  surface brightness radial profile. The  $e_{\text{weight}}$  values are calculated with a 1-arcsec region centred on the quasar masked out to avoid residuals from point-spread function subtraction.

The Arrigoni Battaia et al. (2019) sample consists of 61 luminous blue quasars of median  $z = 3.2$  and median bolometric luminosity  $10^{47.4}$  erg s<sup>-1</sup>. For each halo we estimate its maximum linear size as the sum of maximal radial extent from quasar plus  $\sqrt{(\text{covered area})/\pi}$ . We adopt their sample average Ly $\alpha$  surface brightness radial profile. The  $e_{\text{weight}}$  values are calculated with the central 1-arcsec region masked.

The Borisova et al. (2016) sample consists of 19 luminous blue quasars of median  $z = 3.2$  and median bolometric luminosity  $10^{47.6}$  erg s<sup>-1</sup>. We adopt their sample median Ly $\alpha$  surface brightness radial profile as obtained from Marino et al. (2019). The  $e_{\text{unweight}}$  values of this sample are obtained from Mackenzie et al. (2021). They are calculated with a 1-arcsec region centred on the quasar masked.

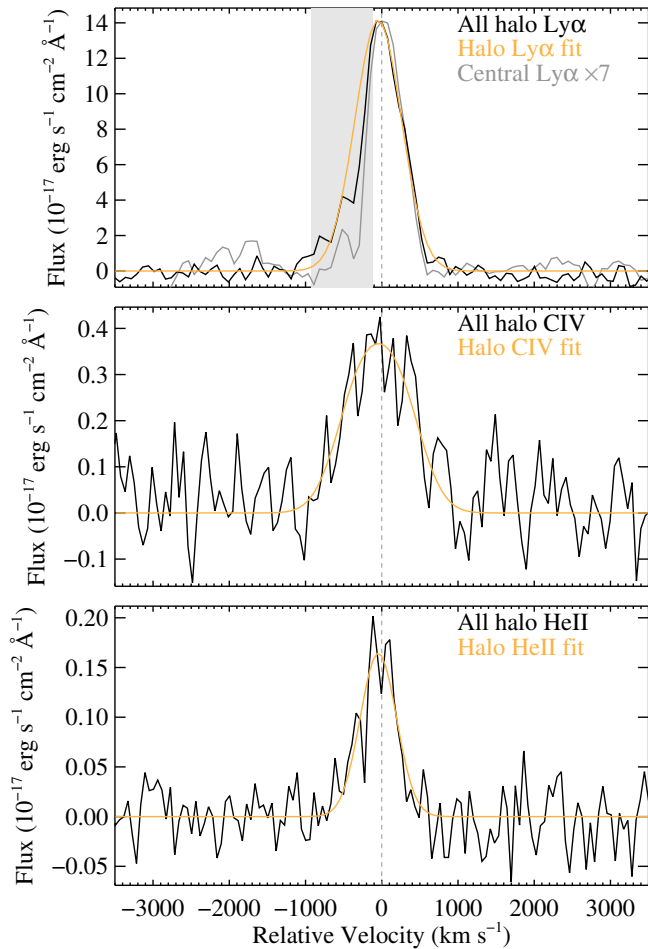


**Figure 8.** Spatially-integrated, one-dimensional spectra of the extended line emissions. The spectra are extracted over areas covered by the three-dimensional segmentation masks collapsed in the spectral direction. Grey dashed lines mark locations of zero velocities. Top panel shows Ly $\alpha$ . The black is the data. The orange curve is a single Gaussian fit to the data. During the fitting the absorption on the blue side of the line profile is masked, and is shaded in grey. The grey curve is the narrow Ly $\alpha$  emission region of a 1-arcsec aperture spectrum centred on the quasar minus a fit to the local pseudo-continuum underneath it. The peak flux of this central 1-arcsec spectrum is rescaled to match the peak of the halo emission for comparison. Middle panel shows C IV  $\lambda\lambda 1548,1550$ . The orange curve is a tied double Gaussian fit to the data. Bottom panel shows He II  $\lambda 1640$ . The orange curve is a single Gaussian fit to the data.

The Guo et al. (2020) sample consists of 80 luminous blue quasars of median  $z = 3.2$  and median bolometric luminosity  $10^{47.5}$  erg s $^{-1}$ . It is the combined sample of Arrigoni Battaia et al. (2019) and Borisova et al. (2016). We adopt their sample stacked C IV  $\lambda 1549$  surface brightness radial profile. We adopt their sample stacked C IV  $\lambda 1549$ /Ly $\alpha$  and He II  $\lambda 1640$ /Ly $\alpha$  ratios of an inner region  $\sim 20$  kpc in size.

The Mackenzie et al. (2021) sample consists of 12 fainter blue quasars of median  $z = 3.2$  and median bolometric luminosity  $10^{47.0}$  erg s $^{-1}$ . We adopt their sample average Ly $\alpha$  surface brightness radial profile. The  $e_{\text{unweight}}$  values are calculated with the central 1-arcsec region masked.

The den Brok et al. (2020) sample consists of four radio-quiet Type II active galactic nuclei of median  $z = 3.4$  and median intrinsic

bolometric luminosity  $10^{46.7}$  erg s $^{-1}$ . The sources are X-ray selected. We verify that the intrinsic bolometric luminosities estimated based on measured mid-IR luminosities are similar to those estimated based on measured X-ray luminosities and the correction factors modeled in Shen et al. (2020). We measure the maximum linear sizes of the Ly $\alpha$  haloes by hand on the maps. Two of their sources have significantly longer exposure times than J0006+1215 and their sizes are omitted in the comparison. We adopt the individual Ly $\alpha$  surface brightness radial profiles of the sources. As their sources are obscured, no point-spread function subtraction is needed to reveal halo emissions. C IV  $\lambda 1549$ /Ly $\alpha$  ratios are not reported and we plot them as lower limits above zero. For two of their sources which have He II  $\lambda 1640$  maps presented, we measure the He II  $\lambda 1640$ /Ly $\alpha$  ratios by hand in a region  $\sim 10$  kpc in size around the sources. Their  $e_{\text{unweight}}$  values are calculated without masking the centre.

The single source of Marino et al. (2019) is a luminous blue quasar absorbed by a proximate damped Ly $\alpha$  system at  $z = 3.0$ . We adopt the C IV  $\lambda 1549$ /Ly $\alpha$  and He II  $\lambda 1640$ /Ly $\alpha$  ratios of a region  $\sim 20$  kpc in size around the central source.

The single source of Sanderson et al. (2021) is a radio-quiet Type II active galactic nucleus at  $z = 3.2$ . The Ly $\alpha$  halo was discovered before the mid-IR central source was identified. The mid-IR source is not detected in the optical. We adopt the C IV  $\lambda 1549$ /Ly $\alpha$  and He II  $\lambda 1640$ /Ly $\alpha$  ratios of a region  $\sim 20$  kpc in size around the central source. The  $e_{\text{unweight}}$  value is calculated without masking the centre.

The single source of Cai et al. (2017) is a radio-quiet Type II active galactic nucleus at  $z = 2.3$ . We adopt the C IV  $\lambda 1549$ /Ly $\alpha$  and He II  $\lambda 1640$ /Ly $\alpha$  ratios of a region  $\sim 10$  kpc in size that is offset by 15 kpc from the source.

In general, measurements that describe an entire halo are not sensitive to masking the central 1 arcsec of the Ly $\alpha$  halo, which is a necessary procedure for studying haloes powered by blue quasars. It is fair to compare quantities that describe the overall halo of J0006+1215 and haloes in the literature. In J0006+1215, the central source is obscured, allowing views of the innermost halo region which is not possible with blue quasars. As demonstrated in Mackenzie et al. (2021), even for fainter blue quasars, uncertain point-spread function subtraction can dilute physical trends between quasar properties and halo properties on scales  $\lesssim 20$  kpc from the quasar. Comparing quantities that are sensitive to the inner halo requires caution.

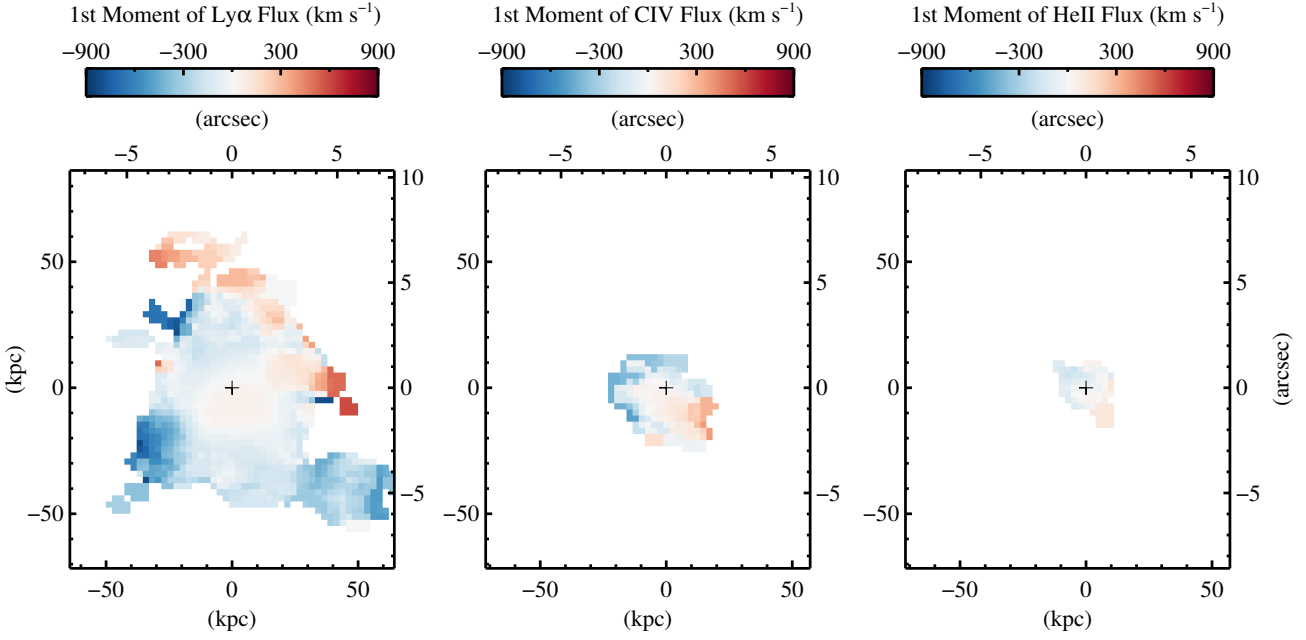
### 3.5.2 The Comparison Results

Fig. 12 compares J0006+1215's Ly $\alpha$  halo luminosity with sources from the literature. We have verified that the calculated Ly $\alpha$  halo luminosities of J0006+1215 without and with masking the central 1 arcsec are very similar, and the central 1-arcsec line luminosity is only 10 per cent of the total. Thus we may compare Ly $\alpha$  halo luminosities of different sources despite that the innermost halo emissions of some of them cannot be recovered. Considering only the Type I blue quasars in the figure, halo line luminosity weakly increases with quasar bolometric luminosity with substantial scatter in the trend. If one fits a linear relation between the halo luminosities and bolometric luminosities of the Type I blue quasars, the measured halo luminosity of J0006+1215 would be  $\sim 0.3$  times the prediction from this relation. This factor of three deficit in halo luminosity for J0006+1215 is well within the scatter around the trend between halo luminosity and bolometric luminosity.

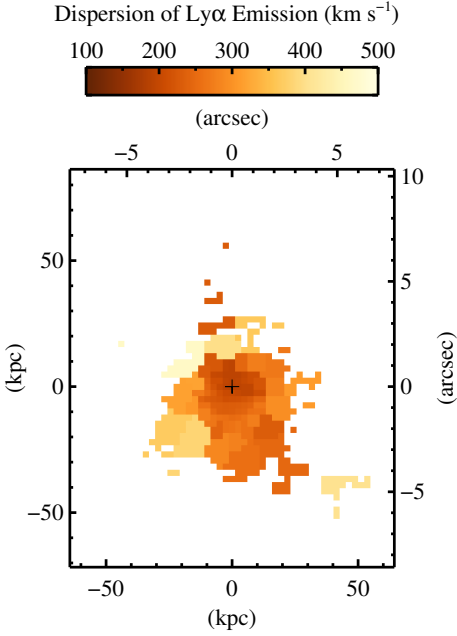
Fig. 13 compares J0006+1215's halo maximum linear size with sources from the literature. The J0006+1215 halo's extent is not outstanding.

Fig. 14 compares J0006+1215's flux-weighted elliptical eccentric-





**Figure 9.** Line velocity centroid maps of Ly $\alpha$ , C IV  $\lambda$ 1549, and He II  $\lambda$ 1640, obtained as the first velocity moments of the line flux distributions. For each emission line, the values are calculated using only voxels that are significantly detected, i.e. selected by the three-dimensional segmentation mask.



**Figure 10.** Ly $\alpha$  velocity dispersion map, obtained by fitting Gaussians on Voronoi-binned data.

ity with sources from the literature. Since  $e_{\text{weight}}$  is sensitive to inner halo emission, for fairer comparison with blue quasars we show both the J0006+1215  $e_{\text{weight}}$  value calculated with the full Ly $\alpha$  halo, 0.44, and that calculated with the central 1 arcsec masked, 0.50. Both calculations yield a low value relative to other sources. The J0006+1215 inner halo is more circularly symmetric than the inner haloes of most luminous blue quasars.

Fig. 15 compares J0006+1215’s flux-unweighted elliptical eccentricity with sources from the literature. Our comparison holds despite that the innermost halo emissions of some of the literature sources

cannot be recovered, since the overall halo eccentricity is insensitive to the innermost emission. For J0006+1215, without or with masking the central 1 arcsec yields nearly the same  $e_{\text{unweight}}$ . The J0006+1215 halo’s overall morphology is similarly asymmetric to the average of haloes surrounding luminous blue quasars and fainter blue quasars, and is less asymmetric than the average of haloes surrounding Type II active galactic nuclei.

Fig. 16 compares the fit to J0006+1215’s Ly $\alpha$  surface brightness radial profile and the fit to J0006+1215’s C IV  $\lambda$ 1549 surface brightness radial profile with sources from the literature. The obscuration in J0006+1215 allows tracing the innermost region of the halo, which is not possible for normal blue quasars whether faint or luminous. The exponential function fit to the J0006+1215 Ly $\alpha$  halo profile has a relatively small scale length of 8.5 kpc. In contrast the comparison blue quasar samples are described by exponential scale lengths of 10.0 kpc to 18.7 kpc. Relative to blue quasars the J0006+1215 Ly $\alpha$  halo is more centrally concentrated. We note that the smaller scale length of J0006+1215 is not caused by recovering innermost halo emission. Half the FWHM size of the point-spread function in our KCWI data is 0.7 arcsec or 6 kpc, and the comparison data have similar point-spread function sizes. Visual comparison of the surface brightness radial profiles beyond 6 kpc projected distance reveals that the J0006+1215 Ly $\alpha$  profile is indeed steeper. The J0006+1215 C IV  $\lambda$ 1549 profile resembles that of the luminous blue quasars.

Fig. 17 compares J0006+1215’s C IV  $\lambda$ 1549/Ly $\alpha$  and He II  $\lambda$ 1640/Ly $\alpha$  ratios with sources from the literature. The ratios are reported for line fluxes measured over inner regions  $\sim(10\text{--}20)$  kpc in sizes. Compared to the inner haloes around other Type I quasars which have He II  $\lambda$ 1640/Ly $\alpha$  ratios  $\sim(0.01\text{--}0.03)$ , the J0006+1215 inner halo has a similar line ratio. Compared to the inner haloes of radio-quiet Type II active galactic nuclei which have He II  $\lambda$ 1640/Ly $\alpha$  ratios reaching  $\sim 0.1$ , the inner haloes of J0006+1215 and other Type I quasars have lower line ratios.

Fig. 18 compares J0006+1215’s Ly $\alpha$  halo-integrated velocity dispersion with sources from the literature. With typical  $\sigma_{1D}$  values of

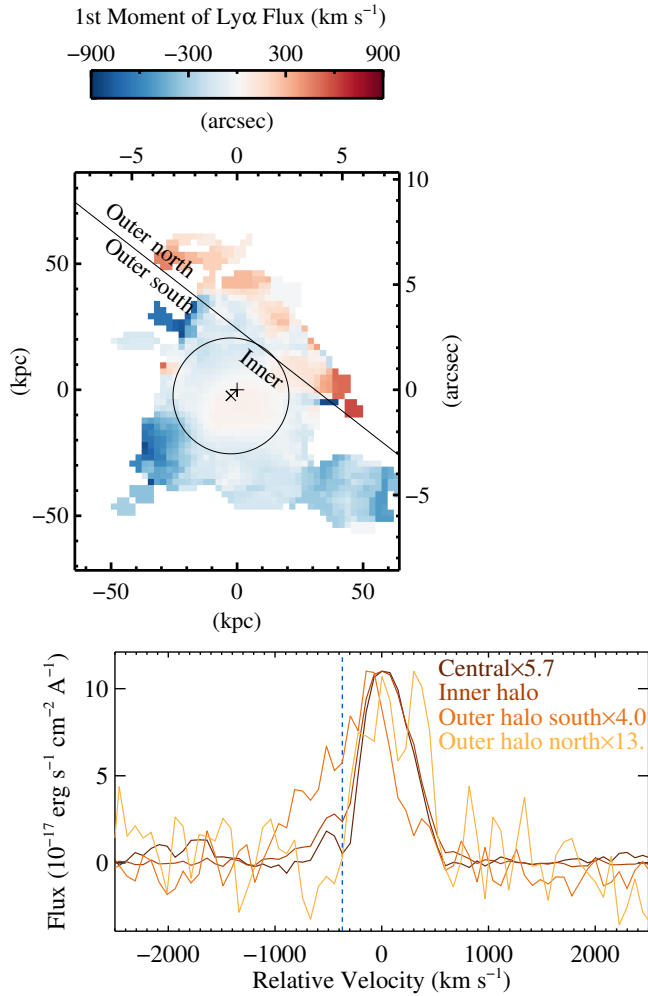


**Figure 11.** One-dimensional spectra extracted from apertures defined using features on the first velocity moment map of  $\text{Ly}\alpha$ . The top panel shows the delineations on the first moment map. The plus symbol marks the quasar position. The cross symbol marks the halo peak. The circle marks an inner halo region of radius 23 kpc extending from the halo peak, where the line-emitting gas is largely at rest relative to the systemic velocity. For the outer halo, a slanted line divides it into a southern region and a northern region along the change from negative to positive velocities. The bottom panel shows the spectra extracted from these three apertures, and we overplot the central 1-arcsec aperture spectrum in the same panel. To facilitate comparison of the profiles, the central 1-arcsec spectrum, the southern outer halo spectrum, and the northern outer halo spectrum are exaggerated. The blue dashed line marks the relative velocity of the absorption trough in the inner halo spectrum.

quasar host dark matter haloes as estimated in Section 3.4 as baseline comparison, the J0006+1215 halo is similarly kinematically quiet to the average of haloes of luminous blue quasars at similar redshifts.

## 4 DISCUSSION

### 4.1 Measuring Quasar Systemic Redshifts

With the aid of dust obscuration in J0006+1215 to reveal narrow line components, in Section 3.4 we show that the redshift and line profile of the narrow component in  $\text{Ly}\alpha$  in the central 1 arcsec match the inner halo emission. Therefore this spike also arises from the

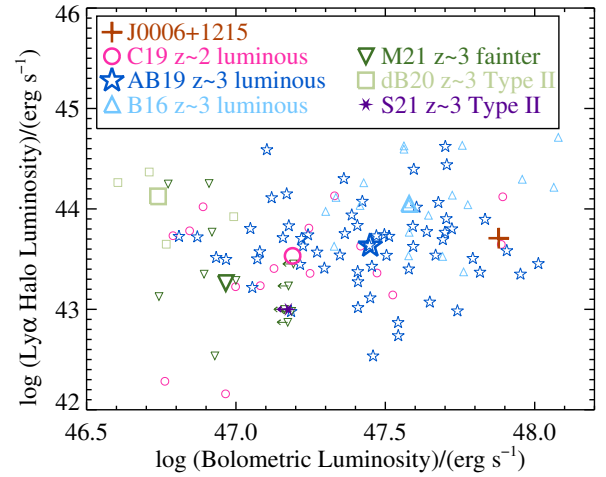


**Figure 12.**  $\text{Ly}\alpha$  halo luminosity against quasar bolometric luminosity, of various literature sources and J0006+1215. Upper limits and lower limits on the quantities are shown with arrows. The brown plus symbol shows J0006+1215. The dark pink circle symbols, the dark blue star symbols, the light blue upward triangle symbols, and the dark green downward triangle symbols show samples of Type I blue quasars. The light green square symbols show a sample of Type II active galactic nuclei. Medians of these literature samples are plotted as larger symbols of the same styles as their individual data points. The dark purple hexagram symbol shows a single Type II source.

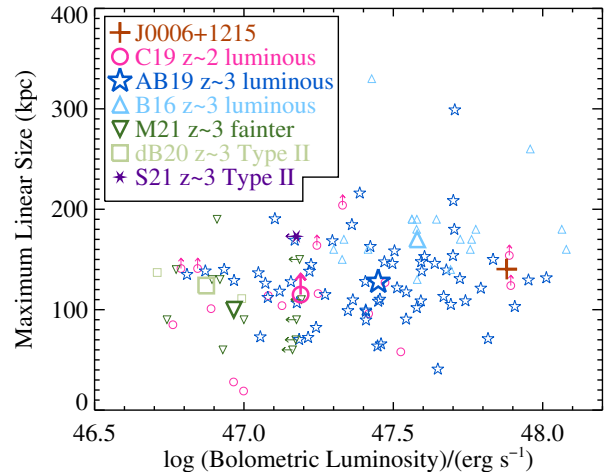


**Figure 13.** Maximum linear size of  $\text{Ly}\alpha$  halo against quasar bolometric luminosity of various literature sources and J0006+1215. The symbology scheme follows Fig. 12.

inner halo region, with the central 1-arcsec emission otherwise dominated by quasar emission. Redshifts and profile widths of the narrow component in the central 1-arcsec  $\text{Ly}\alpha$  and that in the unresolved  $[\text{O III}]\lambda 5007$  are both consistent within one spectral resolution element  $\approx 150 \text{ km s}^{-1}$ . This confirms that narrow  $[\text{O III}]\lambda 5007$  component measured in the central 1-arcsec aperture is also related to the inner halo. These narrow emission lines arising from the kinematically quiet inner halo region should be good indicators of the systemic redshift, and therefore good velocity references for measuring blueshifts in the quasar broad emission lines. This is particularly

**Table 7.** Literature Samples and Single Sources for Comparison

Reference	Sample Size and Source Type	Data Type	Adopted Measurements
Cai et al. (2019)	16 luminous blue quasars	Integral field	Halo luminosity, size, $e_{\text{weight}}$ , average SB profile, velocity dispersion
Arrigoni Battaia et al. (2019)	61 luminous blue quasars	Integral field	Halo luminosity, size, $e_{\text{weight}}$ , average SB profile
Borisova et al. (2016)	19 luminous blue quasars	Integral field	Halo luminosity, size, $e_{\text{unweight}}$ , average SB profile
Guo et al. (2020)	80 luminous blue quasars	Integral field	C IV average SB profile, averageline ratios
Mackenzie et al. (2021)	12 fainter blue quasars	Integral field	Halo luminosity, size, $e_{\text{unweight}}$ , average SB profile
den Brok et al. (2020)	4 Type II AGN	Integral field	Halo luminosity, size, $e_{\text{unweight}}$ , individual SB profiles, individual line ratios
Marino et al. (2019)	Single proximate DLA quasar	Integral field	Line ratios
Sanderson et al. (2021)	Single Type II AGN	Integral field	Halo luminosity, size, $e_{\text{unweight}}$ , SB profile, line ratios
Cai et al. (2017)	Single Type II AGN	Narrowband image	Line ratios

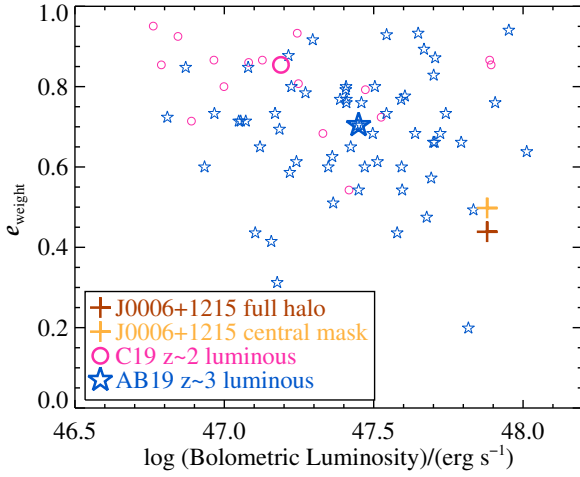


**Figure 14.** Flux-weighted elliptical eccentricity against quasar bolometric luminosity, of various literature sources and J0006+1215. The symboling scheme follows Fig. 12. For J0006+1215, we show both the  $e_{\text{weight}}$  value calculated with the full Ly $\alpha$  halo and that calculated with the central 1 arcsec masked for fairer comparison with blue quasars.

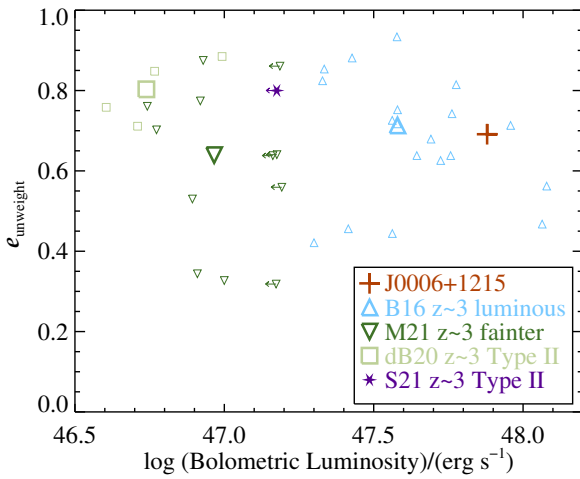


**Figure 15.** Flux-unweighted elliptical eccentricity against quasar bolometric luminosity, of various literature sources and J0006+1215. The symboling scheme follows Fig. 12.

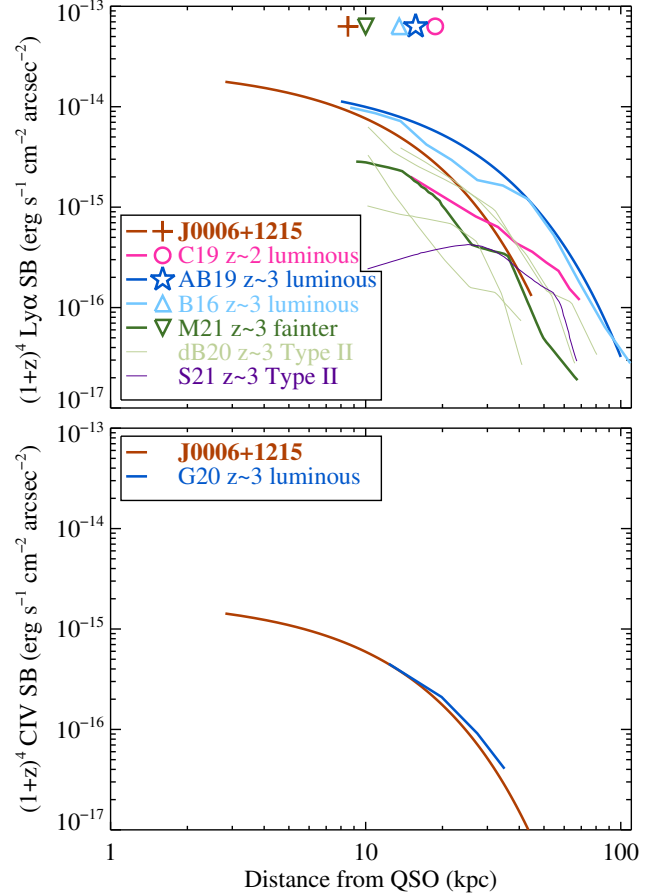


**Figure 16.** Surface brightness radial profiles of Ly $\alpha$  and C IV  $\lambda 1549$  of various literature sources and the exponential fits to the surface brightness radial profiles of Ly $\alpha$  and C IV  $\lambda 1549$  of J0006+1215. Top panel shows Ly $\alpha$ . The brown curve shows J0006+1215. The dark pink curve, the dark blue curve, the light blue curve, and the dark green curve are averages of samples of Type I blue quasars. The thin light green curves are four different sources from a sample of Type II active galactic nuclei. The thin dark purple curve is a single Type II source. Near the top edge of this panel we plot the exponential scale lengths of the blue quasar samples and J0006+1215. Bottom panel shows C IV  $\lambda 1549$ . The brown curve shows J0006+1215. The dark blue curve is the stack a sample of luminous blue quasars. Axes of the bottom panel displays the same data ranges as the top panel. displays All surface brightnesses are corrected for cosmological dimming.

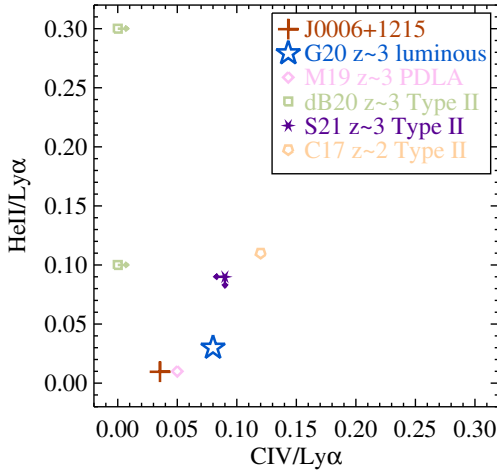


**Figure 17.** He II  $\lambda 1640/Ly\alpha$  ratio against CIV  $\lambda 1549/Ly\alpha$  ratio spatially integrated over inner halo regions where both lines are significantly detected, of various literature sources and J0006+1215. The brown plus symbol shows J0006+1215. The large dark blue star symbol shows the stack of a sample of Type I blue quasars. The light pink diamond symbol shows a single Type I blue quasar. The light green square symbols, the dark purple hexagram symbol, and light orange downward pentagon symbol show Type II sources from different studies. Both data axes show the same range to keep a 1:1 aspect ratio.

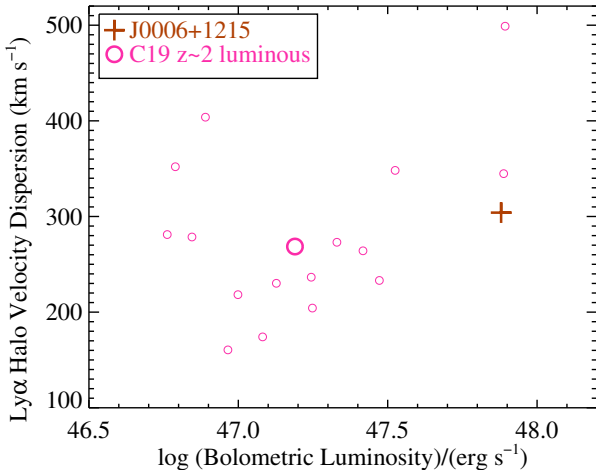


**Figure 18.** Spatially integrated velocity dispersion of the Ly $\alpha$  halo emission against quasar bolometric luminosity, of literature sources and J0006+1215. The brown symbol shows J0006+1215. The dark pink symbols show a sample of luminous blue quasars, whose median is plotted as a larger symbol of the same style.

helpful for an ERQ, as blueshifts are larger and more pervasive across different rest-frame UV lines than normal blue quasars. In J0006+1215, the broad CIV  $\lambda 1549$ 's velocity centroid is blueshifted by  $2240 \text{ km s}^{-1}$ .

If the expectation of no large velocity shifts between the haloes and the systemics generally applies, then narrow features in quasar spectra can accurately reveal large blueshifts in the broad emission lines. Having access to more reliable estimates of systemic redshifts also

allows studying quasar-powered haloes with the narrowband imaging technique, which had missed quasar-powered haloes in previous studies (e.g., Arrighi Battaia et al. 2016). For intermediate to high redshift quasars, whose spectral data are often limited to rest-frame UV wavelengths, their systemic redshifts are often estimated based on broad emission lines and are uncertain by hundreds of  $\text{km s}^{-1}$ . This explains why literature samples often find large differences between the Ly $\alpha$  halo redshifts and the estimated systemic redshifts. For fainter blue quasars, Mackenzie et al. (2021) find that the velocity of the peak of a quasar's Ly $\alpha$  line traces the velocity centroid of the Ly $\alpha$  halo better than any other estimates of the quasar systemic. Our finding that a Ly $\alpha$  spike in the ERQ spectrum is inner halo emission is consistent with their speculation that the narrow peak of a fainter blue quasar's Ly $\alpha$  line is due to contribution from the halo.

## 4.2 Measuring the Inner Circumgalactic Medium

Enabled by the obscuration in J0006+1215, Figs 3 and 4 show that the narrow H I Ly $\alpha$  spike arising from the inner halo is kinematically distinct from the quasar's broad Ly $\alpha$  emission line. We are able to study surface brightnesses, morphologies, and spatially resolved kinematics of three halo emission lines down to zero projected distance from the quasar position.

In Sections 3.2 and 3.4 we show there are no abrupt changes in the innermost regions of the Ly $\alpha$  surface brightness map and velocity maps. This suggests a smooth transition between the interstellar medium and the inner circumgalactic medium, consistent with the finding in Marino et al. (2019) where a proximate damped Ly $\alpha$  system absorbs the glare of the quasar. The emission from their proximate damped Ly $\alpha$  system dominates the inner halo region, however. We contend that the halo emission surrounding J0006+1215 is more representative of the more general population of quasar-powered haloes.

From the line ratio maps in Section 3.3 we find that both the CIV  $\lambda 1549/Ly\alpha$  and He II  $\lambda 1640/Ly\alpha$  ratios are higher near the quasar than further away. Some measurements on line-emitting haloes in the literature show lower CIV  $\lambda 1549/Ly\alpha$  or He II  $\lambda 1640/Ly\alpha$  at small distances of (1–2) arcsec from their quasars than further away (e.g., Marino et al. 2019; Travascio et al. 2020). It is possible that for blue quasars, extraction of narrow CIV  $\lambda 1549$  or He II  $\lambda 1640$  is more prone to oversubtracting the unresolved quasar than extraction of narrow Ly $\alpha$ , due to their fainter nature. We caution that interpretations of spatial gradients of line ratios in inner halo regions need to take into account of uncertainties from oversubtraction.

We show that the halo emission properties transition near a distance of  $\sim(20\text{--}30)$  kpc from the centre. The morphology analysis in Section 3.2 shows that the halo emission is more circularly symmetric in the inner region and appears filamentary in the outer region. The line ratio analysis in Section 3.3 shows that metal enrichment is present in the inner region. The kinematics analysis in Section 3.4 shows that, the velocity field is more coherent and more quiet in the inner halo, and shows more shear and higher dispersion in the outer halo. The kinematics analysis further shows that, a blueshifted absorption feature is present in the inner-halo Ly $\alpha$  line profile, and is absent in the outer-halo line profile.

Evidence of a transition in gaseous properties from inner halo to outer halo regions has been reported in the literature for other samples. Chen et al. (2020) use projected galaxy-galaxy pairs to study gaseous haloes of  $z \sim 2$  star forming galaxies in absorption. They find that outflows at radial speeds  $\sim 600 \text{ km s}^{-1}$  dominate the absorption signals at projected distances within  $\sim 50$  kpc and inflows dominate at larger projected distances. The limitation with background sight-line absorption spectroscopy is that sensitivity to the innermost halo



region is lacking. [Chen et al. \(2021\)](#) observe the gaseous haloes of  $z \sim 2$  star forming galaxies in emission with KCWI. They find that outflows of radial speeds at several hundred  $\text{km s}^{-1}$  dominate on distance scales out to  $\sim 30$  kpc from the central galaxies. Their extended emissions are predominantly only powered by scattering of centrally generated photons, thus it is very challenging to detect any transition in halo emission properties on scales  $\sim 30$  kpc and beyond around inactive galaxies. [Li et al. \(2021\)](#) study a single bright Ly $\alpha$  halo at  $z \sim 3$  suspectedly powered by a central source. They find that outflows at radial speeds  $\sim 600 \text{ km s}^{-1}$  dominating within  $\sim 30$  kpc from the centre that transition to inflows dominating distance scales beyond. The central powering source is not detected however, possibly due to dust extinction or contamination by a foreground source. [Guo et al. \(2020\)](#) stack integral-field spectroscopy data of  $z \sim 3$  luminous blue quasars, and find the average metallicity is about constant within  $\sim 40$  kpc from the central quasars and declines sharply beyond that. The limitation with studying blue quasars is again the lack of sensitivity to the innermost halo region. While the estimated distance scales of inner versus outer halo may vary with the sensitivity of the data and the diverse quasar/galaxy environments, a picture of a two-component circumgalactic medium is emerging from the literature. This two-component nature of the circumgalactic medium, has also been observed around a radio galaxy ([Vernet et al. 2017](#)). The J0006+1215 results strengthen this picture of moderate-speed outflow dominating inner halo and inflow dominating outer halo.

### 4.3 No Prominent Dependence between Halo Emission and Quasar Colour

In Section 3.5.2 we show that the size, line luminosity, and kinematics measured on the J0006+1215 H I Ly $\alpha$  halo are within the wide, diverse ranges measured for Ly $\alpha$  haloes around blue quasars of matching luminosities and redshifts. These comparisons suggest that the quasar illumination pattern in the circumgalactic medium and the circumgalactic medium properties of J0006+1215 are broadly similar to those of luminous blue quasars, and are not prominently affected by its quasar colour.

In Section 3.5.2 we do find that J0006+1215 has a more centrally concentrated halo and a more circularly symmetric inner halo, with implications that we discuss below.

### 4.4 Youth of the ERQ

Fig. 16 compares surface brightness radial profiles and shows that the J0006+1215 Ly $\alpha$  halo is more centrally concentrated. Fig. 14 compares flux-weighted elliptical eccentricities, which are more sensitive to inner halo morphologies, shows that the inner region of the J0006+1215 Ly $\alpha$  halo has a more symmetric appearance. The higher central concentration of the surface brightness and the more symmetric appearance of the inner halo are consistent with the ERQ being in an earlier stage of evolution than luminous blue quasars at similar redshifts. As evident from the C IV  $\lambda 1549$  detection, outflow materials centrally driven by a previous quasar episode or star formation are present in the inner halo. If the ERQ is younger, there is less time for outflow materials to expand to outer halo regions. The inner halo is then loaded with Ly $\alpha$ -emitting gas, and this gas of outflow origin lacks the asymmetric morphology characteristic of inflowing streams.

[Perrotta et al. \(2019\)](#) measure that ERQs show systematically more extreme [O III]  $\lambda 5007$  kinematics than blue quasars matched in luminosities and redshifts. Further, among ERQs the extreme

[O III]  $\lambda 5007$  kinematics positively correlates with the red  $i - W3$  quasar colour. In spite of that, in Section 3.5.2 we show that the Ly $\alpha$  halo kinematics of J0006+1215 is similar to luminous blue quasars. A lack of dependence of Ly $\alpha$  halo kinematics on quasar colour does not bear implications on the dependence between quasar evolutionary stage and colour, however. The quiet kinematics indicate that any Ly $\alpha$ -emitting materials swept by quasar-driven outflows slow to moderate speeds on halo scales in J0006+1215 and in luminous blue quasars. The adaptive optics-assisted data in [Vayner et al. \(2021\)](#) show that the extreme [O III]  $\lambda 5007$  outflows of ERQs happen within  $\sim 1$  kpc radii. Their result is consistent with our wide-field data that show no broadening in Ly $\alpha$  in J0006+1215 down to  $\sim 0.7$  arcsec or  $\sim 6$  kpc radius. Lifetimes of quasar episodes as measured by their proximity zones are typically  $(10^5 - 10^7)$  yr (e.g., [Khrykin et al. 2021](#)). Even if an observed episode has been on for  $10^7$  yr, for a characteristic outflow speed consistent with the kinematics of most Ly $\alpha$  haloes  $\sim 400 \text{ km s}^{-1}$ , an outflow driven by the episode can only travel out to  $\sim 4$  kpc. Any Ly $\alpha$ -emitting materials on circumgalactic scales of outflow origin are thus not driven by the observed quasar episode but in the past. The absence of fast circumgalactic Ly $\alpha$  outflows in J0006+1215 has no implications on the quasar evolutionary stage.

### 4.5 Quasar Illumination Beyond Orientation Effects

A fundamental question about the nature of ERQs is whether their obscuration is due to orientation effects or a global dust distribution. Orientation effects may be caused by a dusty torus and axisymmetric ionization cones as often invoked to explain the Type I/Type II dichotomy. On the other hand a more global dust distribution may relate to ERQs residing in more dusty and younger host galaxies than other luminous quasars. One unusual feature of ERQs is that their spectral energy distributions are typically nearly flat in the rest-frame UV despite having extremely red colours from rest-frame UV to mid-IR. This spectral shape is not consistent with normal galactic reddening curves. It appears to require global patchy dust distributions ([Hamann et al. 2017](#)), unusually large dust grain sizes as observed in the envelope ejecta of some massive evolved stars and supernovae ([Hamann 2012; Di Mascia et al. 2021](#)), or a significant contribution from scattered rest-frame UV continuum light ([Alexandrov et al. 2018](#)). We note that the KCWI data probe illumination pattern on circumgalactic scales, not obscuration geometry on circumnuclear scales. Our data do not distinguish between ionizing photons escaping through a global patchy dust distribution along the line of sight or scattering off an anisotropic dust distribution and then escaping along the line of sight. In the following we explain that the Ly $\alpha$  halo properties of J0006+1215 suggest unique physical conditions for this ERQ that are beyond orientation differences from other known quasar populations.

Figs 12 and 13 show that the line luminosity and linear size of the J0006+1215 H I Ly $\alpha$  halo are well within the ranges spanned by other Type I and Type II quasar-powered Ly $\alpha$  haloes. The Ly $\alpha$  halo luminosity of J0006+1215 is only moderately suppressed compared to similarly intrinsically luminous blue quasars. A lack of a trend between halo sizes or halo luminosities and quasar colours can be explained if the halo emissions around quasars are not predominantly ionization-bounded ([Dempsey & Zakamska 2018](#)). The amount of halo emission will then only weakly depend on the amount of ionizing radiation or obscuration. The only moderately suppressed halo luminosity of J0006+1215 thus does not imply that J0006+1215 has globally minimal extinction for ionizing photons, as would be the case if J0006+1215 were no different from a blue quasar other than orientation. In addition, it has been measured that obscured quasars reside in more massive dark matter haloes ([DiPompeo et al. 2017](#);

Geach et al. 2019). Obscured quasars would then have larger amounts of halo gas to fluoresce in Ly $\alpha$ , which would counteract global extinction effects of ionizing photons.

Fig. 17 shows that the low He II  $\lambda$ 1640/Ly $\alpha$  ratio of the J0006+1215 inner halo is closer to those measured for inner haloes around Type I sources and is lower than those of inner haloes around Type II sources. Cantalupo et al. (2019) discuss how the He II  $\lambda$ 1640/Ly $\alpha$  ratio gives clue to the observed illuminated volume of a quasar. Considering that the brightness of the high-ionization He II  $\lambda$ 1640 line declines with physical distance more steeply than Ly $\alpha$ , for a given projected area around a quasar, lower He II  $\lambda$ 1640/Ly $\alpha$  ratio implies higher Ly $\alpha$  fluorescent volume. A quasar episode has finite lifetime, resulting in light travel effects. Under the Type I/Type II dichotomy, the observed Ly $\alpha$  fluorescent volume of a Type I source which beams along the line of sight is much larger than that of Type II source which beams in the plane of the sky. For a Type I source, the physical distances spanned by the ionized gas are much larger than their sky projected distances. The He II  $\lambda$ 1640/Ly $\alpha$  ratio at a given projected distance from a Type I source is then lower than that from a Type II source. It is intriguing that the J0006+1215 inner halo has a Type I-like He II  $\lambda$ 1640/Ly $\alpha$  ratio despite our inference that the ionizing radiation is weaker along the line of sight than in the plane of sky. The low He II  $\lambda$ 1640/Ly $\alpha$  ratio implies the observed Ly $\alpha$  fluorescent volume along the line of sight is still larger than in the plane of the sky, which is possible when the fluorescent Ly $\alpha$  emission is not predominantly ionization-bounded. In turn this implies that the central ionizing photons have certain channels to escape along the line of sight.

Fig. 15 shows that the overall morphology of the J0006+1215 Ly $\alpha$  halo is more circularly symmetric than all haloes around Type II sources. In den Brok et al. (2020) it is suggested that under the Type I/Type II dichotomy the different orientations of the ionization cones imply that Type II sources should power haloes that appear more asymmetric than Type I-powered haloes. The Type I-like halo morphology of J0006+1215 is consistent with the scenario that ionizing photons can escape along the line of sight.

The Type I-like halo properties of J0006+1215 are consistent with the appearance of broad emission lines in the quasar spectrum clearly shown in Fig. 1 despite extremely red colour.

We note that Goulding et al. (2018) find the X-ray absorbing column toward J0006+1215 is in the Compton-thin regime, and hence does not suggest anisotropic obscuration.

#### 4.6 No Evidence of Fast-moving and Ly $\alpha$ -emitting Halo Gas

In Section 3.4 we show that the J0006+1215 inner halo is kinematically quiet with respect to the estimated dark matter velocity dispersion. In theory, fast-moving and Ly $\alpha$ -emitting halo gas are not necessarily expected in radio-quiet quasars at cosmic noon. In the cosmological radiation-hydrodynamic simulations of Costa et al. (2022), the quasar-driven outflowing gas that moves at  $\sim 1000$  km s $^{-1}$  on circumgalactic scales is in a much less dense phase than the bulk of the Ly $\alpha$ -emitting gas. It is very possible that supermassive black hole feedback on the circumgalactic medium becomes observationally evident and are required by cosmological hydrodynamic simulations only after  $z \lesssim 2$  (Nelson et al. 2019; Sorini et al. 2020, 2021). An analytical model also proposes that supermassive black hole feedback gently lifts the circumgalactic medium and never manifests as fast circumgalactic outflows (e.g., Voit et al. 2020).

At present, no selection criteria on extreme properties of radio-quiet quasars systematically find fast-moving and Ly $\alpha$ -emitting halo gas that are way above the dark matter velocity dispersion and require driving by quasars. Although fast Ly $\alpha$  halo gas is occasionally

detected around single blue quasars, the selection criteria of those quasars do not routinely find fast Ly $\alpha$  halo gas. For example, Ginolfi et al. (2018) select a  $z \sim 5$  quasar by its broad absorption lines, and finds high velocity dispersion in the inner Ly $\alpha$  halo. However, the broad absorption line quasar in the  $z > 5.7$  sample of Farina et al. (2019) does not reveal extended emission. Another example is that Travascio et al. (2020) select two quasars by their hyperluminosities, and finds high velocity dispersion in the inner Ly $\alpha$  halo. However, the five hyperluminous quasars among the samples of Cai et al. (2019), Arrigoni Battaia et al. (2019), and Borisova et al. (2016) do not display high velocity dispersion in their Ly $\alpha$  haloes. It appears that the only selection criterion on central powering source properties that systematically finds fast Ly $\alpha$  halo gas is radio loudness, presumably associated with jets that extend outside the host galaxies (Swinbank et al. 2015; Kolwa et al. 2019; Wang et al. 2021).

#### 4.7 Future Work

The full KCWI sample of ERQs (J. Gillette et al. in preparation) is needed to sustain the findings in this work. We suggest three lines of future work. Firstly, search for fainter, redder quasars that are analogues to the dusty first quasars, follow up on their extended emissions, and compare with Ly $\alpha$  haloes of the first quasars. Being young and more globally dusty than typical  $z \sim 2-4$  blue quasars, together with a characteristic spectral energy distribution and thus peculiar extinction properties, it is possible that ERQs are analogues of the majority of the first quasars. Hamann et al. (2017) argue for a scenario where ERQs drive high-speed outflows that ablate and disperse dusty molecular clouds in their host galaxies, resulting in small dusty clumps capable of patchy obscuration on galactic scales. Ni et al. (2022) investigate quasar obscuration in a cosmological hydrodynamic simulation, and find that at  $z \gtrsim 6$  much of the obscuration is on galactic scales, i.e. does not follow the Type II geometry. Di Mascia et al. (2021) investigate obscuration at  $z \sim 6$  in cosmological hydrodynamic simulations, and find a shallow extinction curve. Yung et al. (2021) predict UV luminosity functions of active galactic nuclei in a semi-analytic model, and finds that dust attenuation effects are increasingly suppressed at higher redshifts. To date, Ly $\alpha$  halo surrounding one  $z \sim 6$  obscured quasar has been detected (Connor et al. 2019; Farina et al. 2019). Our second suggestion is to search for signatures of quasar feedback on circumgalactic scales other than fast flows, especially at later cosmic times. Our third suggestion is to search for quasar-driven outflows in line absorption which is more sensitive to underdense gas than line emission.

## 5 CONCLUSIONS

We present a detailed study of KCWI integral field spectroscopic observations of the reddest ERQ, J0006+1215 at  $z_{\text{sys}} = 2.3184$ . It has an  $i - W3$  colour of 8.01, drives unusually fast [OIII]  $\lambda$ 5007-emitting outflows on  $\sim 1$  kpc scale, and exhibits narrow H I Ly $\alpha$  emission in the central 1-arcsec that is otherwise dominated by quasar emission. We analyse the central 1-arcsec spectrum and the spatially resolved properties of the line-emitting halo.

We summarize analysis results on the data as follows:

- The central 1-arcsec spectrum demonstrates narrow line emissions in Ly $\alpha$ , C IV  $\lambda$ 1549,1550, and He II  $\lambda$ 1640 that have similar peak velocities and velocity widths. We take the peak of the Ly $\alpha$  spike to be the systemic redshift. We detect extended Ly $\alpha$  and C IV  $\lambda$ 1549 and marginally spatially resolved He II  $\lambda$ 1640 emissions.

- The maximum linear size of detectable Ly $\alpha$  emission is 140 kpc and that of C IV  $\lambda$ 1549 is 47 kpc. The total Ly $\alpha$  halo luminosity is  $5.10 \times 10^{43}$  erg s $^{-1}$ . For the Ly $\alpha$  halo the flux-weighted elliptical eccentricity with respect to the halo centroid  $e_{\text{weight}} = 0.44$  and the unweighted eccentricity with respect to the quasar position  $e_{\text{unweight}} = 0.69$ . The halo appears circularly symmetric in the inner region and demonstrates some filamentary asymmetry on larger scales. The circularly averaged Ly $\alpha$  surface brightness radial profile is centrally concentrated, and is best fitted by  $\text{SB}_{\text{Ly}\alpha}(r) = (2.46 \times 10^{14}) \times \exp(-r/(8.5 \text{ kpc})) \text{ erg s}^{-1} \text{ cm}^{-2} \text{ arcsec}^{-2}$ . Where both lines in a line ratio are detected, the spatially-integrated ratios C IV  $\lambda$ 1549/Ly $\alpha = 0.03$  and He II  $\lambda$ 1640/Ly $\alpha = 0.01$ .

- The kinematics of the extended emissions are quiet, demonstrating no broadening above the dark matter circular velocity down to the spatial resolution  $\sim 0.7$  arcsec or  $\sim 6$  kpc from the quasar. On the Ly $\alpha$  map, the spatial median of the velocity centroids of detected spaxels is  $-82 \text{ km s}^{-1}$ , with a spatial standard deviation of  $234 \text{ km s}^{-1}$ . On the Ly $\alpha$  map, the spatial median of the velocity dispersions of detected spaxels is  $287 \text{ km s}^{-1}$ , with a spatial standard deviation of  $70 \text{ km s}^{-1}$ . The peak velocities and velocity widths of the spatially-integrated Ly $\alpha$ , C IV  $\lambda$ 1549, and He II  $\lambda$ 1640 emissions are similar to each other. The inner halo emission is kinematically coherent and has blueshifted Ly $\alpha$  absorption, while the outer halo shows kinematic shear and has no blueshifted absorption.

- The narrow Ly $\alpha$  line profile in a central 1-arcsec aperture and that in the inner halo region are very similar. We confirm that the Ly $\alpha$  spike first identified in the BOSS spectrum is an inner extension of the halo emission, and is therefore useful as an indicator of the systemic redshift. Relative to this halo frame, the broad C IV  $\lambda$ 1549 emission in the quasar is blueshifted by  $2240 \text{ km s}^{-1}$ .

- The size, line luminosity, and kinematics of the J0006+1215 Ly $\alpha$  halo are within ranges spanned by luminous blue quasars at similar redshifts, with the halo luminosity being only moderately suppressed relative to blue quasars. The J0006+1215 halo is more centrally concentrated and has a more circularly symmetric inner region compared to these other haloes.

- The J0006+1215 inner halo has as low He II  $\lambda$ 1640/Ly $\alpha$  ratio as other Type I quasars, which is lower than Type II sources. The J0006+1215 overall halo morphology is as asymmetric as other Type I quasars, and less asymmetric than Type II sources.

We summarize our inferences from the data analysis as follows:

- Obscuration in the ERQ allows views of the innermost halo. The narrow Ly $\alpha$  component in the central 1 arcsec and that in the unresolved [O III]  $\lambda$ 5007 accurately reveal large blueshifts of the broad C IV  $\lambda$ 1549 and broad [O III]  $\lambda$ 5007 in the unresolved quasar.

- Measured properties of the J0006+1215 halo transition near  $\sim 30$  kpc from the centre, with the inner region dominated by moderate-speed outflow driven in the past and the outer region dominated by inflow.

- The quasar illumination pattern and the circumgalactic medium properties of J0006+1215 are broadly similar to those of luminous blue quasars.

- The higher concentration and the more symmetric appearance of the inner region of the J0006+1215 halo are consistent with the ERQ being younger than blue quasars. The Ly $\alpha$ -emitting outflow materials have not expanded to the outer regions. On the other hand the lack of dependence of Ly $\alpha$  halo kinematics on quasar colour despite the strong dependence of kpc-scale [O III]  $\lambda$ 5007 kinematics on quasar colour bears no implication on evolutionary stage.

- As halo emissions are not predominantly ionization-bounded, the only moderately suppressed halo luminosity of J0006+1215 does

not imply its obscuration is only due to orientation effects. The inner halo He II  $\lambda$ 1640/Ly $\alpha$  ratio and the overall halo morphology of J0006+1215 being dissimilar to Type II quasars suggests unique physical conditions for this ERQ that are beyond orientation differences from other quasar populations.

- While the J0006+1215 ERQ dominates the ionization of the circumgalactic medium, we find no evidence of mechanical quasar feedback in the Ly $\alpha$ -emitting halo. No selection criteria on any extreme properties of radio quiet quasars have ever systematically found fast-moving Ly $\alpha$  halo gas that requires driving by the quasars.

## ACKNOWLEDGEMENTS

We are grateful to our collaborator A. Vayner. MWL thanks KCWI instrument team members M. Matuszewski and J. D. Neill for technical support. MWL thanks A. Battaia, Z. Cai, S. Cantalupo, Y. Chen, Y. T. Chow, E. Farina, Y. Guo, E. T. Hamden, Q. Li, Z. Li, and D. B. O'Sullivan for helpful discussions. MWL, FH, and JG acknowledge support from the USA National Science Foundation grant AST-1911066. NLZ is supported at the Institute for Advanced Study by the J. Robert Oppenheimer Visiting Professorship and the Bershadsky Fund, and acknowledges support from NASA ADAP grant 80NSSC21K1569. This research was supported in part by the National Science Foundation under Grant No. NSF PHY-1748958. This work is based on observations made at the W. M. Keck Observatory, which is operated as a scientific partnership between the California Institute of Technology and the University of California. It was made possible by the generous support of the W. M. Keck Foundation. Data presented herein were partially obtained using the California Institute of Technology Remote Observing Facility. The authors wish to recognize and acknowledge the very significant cultural role and reverence that the summit of Mauna Kea has always had within the indigenous Hawaiian community. We are most fortunate to have the opportunity to conduct observations from this mountain.

## DATA AVAILABILITY

The data are available upon request.

## REFERENCES

- Alexandroff R. M., et al., 2018, *MNRAS*, **479**, 4936  
 Antonucci R., 1993, *ARA&A*, **31**, 473  
 Arrigoni Battaia F., Hennawi J. F., Cantalupo S., Prochaska J. X., 2016, *ApJ*, **829**, 3  
 Arrigoni Battaia F., Hennawi J. F., Prochaska J. X., Oñorbe J., Farina E. P., Cantalupo S., Lusso E., 2019, *MNRAS*, **482**, 3162  
 Assef R. J., et al., 2015, *ApJ*, **804**, 27  
 Banerji M., Alaghband-Zadeh S., Hewett P. C., McMahon R. G., 2015, *MNRAS*, **447**, 3368  
 Binney J., Tremaine S., 2008, *Galactic Dynamics: Second Edition*. Princeton University Press  
 Borisova E., et al., 2016, *ApJ*, **831**, 39  
 Bridge C. R., et al., 2013, *ApJ*, **769**, 91  
 Cai Z., et al., 2017, *ApJ*, **837**, 71  
 Cai Z., et al., 2019, *ApJS*, **245**, 23  
 Canalizo G., Stockton A., 2001, *ApJ*, **555**, 719  
 Cantalupo S., Arrigoni-Battaia F., Prochaska J. X., Hennawi J. F., Madau P., 2014, *Nature*, **506**, 63  
 Cantalupo S., et al., 2019, *MNRAS*, **483**, 5188  
 Chen Y., et al., 2020, *MNRAS*, **499**, 1721

- Chen Y., et al., 2021, *MNRAS*, **508**, 19
- Connor T., et al., 2019, *ApJ*, **887**, 171
- Costa T., Sijacki D., Haehnelt M. G., 2014, *MNRAS*, **444**, 2355
- Costa T., Arrigoni Battaia F., Farina E. P., Keating L. C., Rosdahl J., Kimm T., 2022, arXiv e-prints, p. [arXiv:2203.11232](https://arxiv.org/abs/2203.11232)
- Cutri R. M., et al., 2013, Explanatory Supplement to the AllWISE Data Release Products, Explanatory Supplement to the AllWISE Data Release Products
- DeFelippis D., Genel S., Bryan G. L., Nelson D., Pillepich A., Hernquist L., 2020, *ApJ*, **895**, 17
- Dekel A., et al., 2009, *Nature*, **457**, 451
- Dempsey R., Zakamska N. L., 2018, *MNRAS*, **477**, 4615
- Di Mascia F., et al., 2021, *MNRAS*, **503**, 2349
- DiPompeo M. A., Hickox R. C., Eftekhazadeh S., Myers A. D., 2017, *MNRAS*, **469**, 4630
- Eftekhazadeh S., et al., 2015, *MNRAS*, **453**, 2779
- Eisenstein D. J., et al., 2011, *AJ*, **142**, 72
- Farina E. P., et al., 2019, *ApJ*, **887**, 196
- Feltre A., Charlot S., Gutkin J., 2016, *MNRAS*, **456**, 3354
- Finnerty L., et al., 2020, *ApJ*, **905**, 16
- Fumagalli M., Hennawi J. F., Prochaska J. X., Kasen D., Dekel A., Ceverino D., Primack J., 2014, *ApJ*, **780**, 74
- Geach J. E., Peacock J. A., Myers A. D., Hickox R. C., Burchard M. C., Jones M. L., 2019, *ApJ*, **874**, 85
- Ginolfi M., Maiolino R., Carniani S., Arrigoni Battaia F., Cantalupo S., Schneider R., 2018, *MNRAS*, **476**, 2421
- Glikman E., et al., 2022, arXiv e-prints, p. [arXiv:2204.13745](https://arxiv.org/abs/2204.13745)
- Goulding A. D., et al., 2018, *ApJ*, **856**, 4
- Guo Y., et al., 2020, *ApJ*, **898**, 26
- Hamann F., 2012, Physics of the Inner Ejecta. Springer-Verlag, p. 95, [doi:10.1007/978-1-4614-2275-4\\_5](https://doi.org/10.1007/978-1-4614-2275-4_5)
- Hamann F., Kanekar N., Prochaska J. X., Murphy M. T., Ellison S., Malec A. L., Milutinovic N., Ubachs W., 2011, *MNRAS*, **410**, 1957
- Hamann F., et al., 2017, *MNRAS*, **464**, 3431
- Herenz E. C., Hayes M., Scarlata C., 2020, *A&A*, **642**, A55
- Hopkins P. F., Elvis M., 2010, *MNRAS*, **401**, 7
- Hopkins P. F., Hernquist L., Cox T. J., Kereš D., 2008, *ApJS*, **175**, 356
- Humphrey A., Villar-Martín M., Binette L., Raj R., 2019, *A&A*, **621**, A10
- Huscher E., Oppenheimer B. D., Lonardi A., Crain R. A., Richings A. J., Schaye J., 2021, *MNRAS*, **500**, 1476
- Hwang H.-C., Zakamska N. L., Alexandroff R. M., Hamann F., Greene J. E., Perrotta S., Richards G. T., 2018, *MNRAS*, **477**, 830
- Kereš D., Katz N., Fardal M., Davé R., Weinberg D. H., 2009, *MNRAS*, **395**, 160
- Khrykin I. S., Hennawi J. F., Worseck G., Davies F. B., 2021, *MNRAS*, **505**, 649
- Kolwa S., et al., 2019, *A&A*, **625**, A102
- Lau E. T., Nagai D., Kravtsov A. V., 2010, *ApJ*, **708**, 1419
- Lau M. W., Prochaska J. X., Hennawi J. F., 2016, *ApJS*, **226**, 25
- Li Q., et al., 2019, *ApJ*, **875**, 130
- Li Z., Steidel C. C., Gronke M., Chen Y., 2021, *MNRAS*, **502**, 2389
- Li Z., Steidel C. C., Gronke M., Chen Y., Matsuda Y., 2022, *MNRAS*, **513**, 3414
- Liu G., Zakamska N. L., Greene J. E., Nesvadba N. P. H., Liu X., 2013, *MNRAS*, **436**, 2576
- Mackenzie R., et al., 2021, *MNRAS*, **502**, 494
- Marino R. A., et al., 2019, *ApJ*, **880**, 47
- Monadi R., Bird S., 2022, *MNRAS*, **511**, 3501
- Morrissey P., et al., 2018, *ApJ*, **864**, 93
- Munari E., Biviano A., Borgani S., Murante G., Fabjan D., 2013, *MNRAS*, **430**, 2638
- Nelson D., Genel S., Vogelsberger M., Springel V., Sijacki D., Torrey P., Hernquist L., 2015, *MNRAS*, **448**, 59
- Nelson D., et al., 2019, *MNRAS*, **490**, 3234
- Netzer H., 2015, *ARA&A*, **53**, 365
- Ni Y., et al., 2022, *MNRAS*, **513**, 670
- Noboriguchi A., et al., 2019, *ApJ*, **876**, 132
- O’Sullivan D., Chen Y., 2020, arXiv e-prints, p. [arXiv:2011.05444](https://arxiv.org/abs/2011.05444)
- O’Sullivan D. B., Martin C., Matuszewski M., Hoadley K., Hamden E., Neill J. D., Lin Z., Parihar P., 2020, *ApJ*, **894**, 3
- Pâris I., et al., 2017, *A&A*, **597**, A79
- Perrotta S., Hamann F., Zakamska N. L., Alexandroff R. M., Rupke D., Wylezalek D., 2019, *MNRAS*, **488**, 4126
- Prescott M. K. M., Martin C. L., Dey A., 2015a, *ApJ*, **799**, 62
- Prescott M. K. M., Momcheva I., Brammer G. B., Fynbo J. P. U., Møller P., 2015b, *ApJ*, **802**, 32
- Ross N. P., et al., 2013, *ApJ*, **773**, 14
- Ross N. P., et al., 2015, *MNRAS*, **453**, 3932
- Rupke D. S. N., 2014, IFSRED: Data Reduction for Integral Field Spectrographs (ascl:1409.004)
- Rupke D., To A., 2021, IFSFIT: Integral Field Spectroscopy FITting, [doi:10.5281/zenodo.5659520](https://doi.org/10.5281/zenodo.5659520)
- Rupke D. S. N., et al., 2019, *Nature*, **574**, 643
- Sanders D. B., Soifer B. T., Elias J. H., Neugebauer G., Matthews K., 1988, *ApJ*, **328**, L35
- Sanderson K. N., Prescott M. M. K., Christensen L., Fynbo J., Møller P., 2021, *ApJ*, **923**, 252
- Schlafly E. F., Finkbeiner D. P., 2011, *ApJ*, **737**, 103
- Shen X., Hopkins P. F., Faucher-Giguère C.-A., Alexander D. M., Richards G. T., Ross N. P., Hickox R. C., 2020, *MNRAS*, **495**, 3252
- Sorini D., Davé R., Anglés-Alcázar D., 2020, *MNRAS*, **499**, 2760
- Sorini D., Dave R., Cui W., Appleby S., 2021, arXiv e-prints, p. [arXiv:2111.13708](https://arxiv.org/abs/2111.13708)
- Suresh J., Nelson D., Genel S., Rubin K. H. R., Hernquist L., 2019, *MNRAS*, **483**, 4040
- Swinbank A. M., et al., 2015, *MNRAS*, **449**, 1298
- Travascio A., et al., 2020, *A&A*, **635**, A157
- Tumlinson J., Peebles M. S., Werk J. K., 2017, *ARA&A*, **55**, 389
- Urrutia T., Lacy M., Becker R. H., 2008, *ApJ*, **674**, 80
- Vayner A., et al., 2021, *MNRAS*, **504**, 4445
- Vernet J., et al., 2017, *A&A*, **602**, L6
- Vito F., et al., 2019, *A&A*, **628**, L6
- Voit G. M., et al., 2020, *ApJ*, **899**, 70
- Wang W., Wylezalek D., De Breuck C., Vernet J., Humphrey A., Villar Martín M., Lehnert M. D., Kolwa S., 2021, *A&A*, **654**, A88
- Wright E. L., 2006, *PASP*, **118**, 1711
- Wright E. L., et al., 2010, *AJ*, **140**, 1868
- Yung L. Y. A., Somerville R. S., Finkelstein S. L., Hirschmann M., Davé R., Popping G., Gardner J. P., Venkatesan A., 2021, *MNRAS*, **508**, 2706
- Zakamska N. L., et al., 2016, *MNRAS*, **459**, 3144
- Zakamska N. L., et al., 2019, *MNRAS*, **489**, 497
- Zhang S., et al., 2017, *ApJ*, **836**, 86
- den Brok J. S., et al., 2020, *MNRAS*, **495**, 1874

This paper has been typeset from a  $\text{\TeX}/\text{\LaTeX}$  file prepared by the author.